EMG-assisted neuromusculoskeletal models can estimate physiological muscle activations and joint moments across the neck before impacts

Dr Pavlos Silvestros
CAMERA*
Department for Health
University of Bath
Bath, United Kingdom

Dr Claudio Pizzolato
School of Allied Health Sciences
GCORE†
Menzies Health Institute
Griffith University
Queensland, Gold Coast, Australia

Prof David G. Lloyd
School of Allied Health Sciences
GCORE
Menzies Health Institute
Griffith University
Queensland, Gold Coast, Australia

Dr Ezio Preatoni
Department for Health
University of Bath
Bath, United Kingdom

Prof Harinderjit S. Gill
Centre for Therapeutic Innovation
Department of Mechanical Engineering
University of Bath
Bath, United Kingdom

Dr Dario Cazzola‡
CAMERA
Department for Health
University of Bath
Bath, United Kingdom
d.cazzola@bath.ac.uk

Knowledge of neck muscle activation strategies prior to sporting impacts is crucial for investigating mechanisms of severe spinal injuries. However, measurement of muscle activations during impacts is experimentally challenging and computational estimations are not often guided by experimental measurements. We investigated neck muscle activations prior to impacts with the use of electromyography (EMG)-assisted neuromusculoskeletal models. Kinematics and EMG recordings from four major neck muscles of a rugby player were experimentally measured during rugby activities. A subject-specific musculoskeletal model was created with muscle parameters informed from MRI measurements. The model was used in the Calibrated EMG-Informed Neuromusculoskeletal Modelling toolbox and three neural solutions were compared: i) static optimisation (SO), ii) EMG-assisted (EMGa) and iii) MRI-informed EMG-assisted (EMGaMRI). EMGaMRI and EMGa significantly (p¡0.01) outperformed SO when tracking cervical spine net joint moments from inverse dynamics in flexion/extension (RMSE = 0.95, 1.14 and 2.32 Nm) but not in lateral bending (RMSE = 1.07, 2.07 and 0.84 Nm). EMG-assisted solutions generated physiological muscle activation patterns and maintained experimental co-contractions significantly (p¡0.01) outperforming SO, which was characterised by saturation and non-physiological "on-off" patterns. This study showed for the first time that physiological neck muscle activations and cervical spine net joint moments can be estimated without assumed a priori objective criteria prior to impacts. Future studies could use this technique to provide detailed initial loading conditions for theoretical simulations of neck injury during impacts.

1 Introduction

The human cervical spine is a highly complex neuromusculoskeletal system that is susceptible to injuries under various loading conditions. Severe cervical spine injuries are commonly caused during sporting (e.g. contact sport) [1, 2],

*Centre for Analysis of Motion and Entertainment Research and Application

†Griffith Centre of Biomedical and Rehabilitation Engineering

‡Address all correspondence for other issues to this author.

automotive (e.g. car roll-overs) [2–4] and occupational [2] (e.g. falls) accidents that involve impacts. Accidents that lead to neurological impairment at the level of the cervical spine are relatively rare, 40 to 80 per million annually worldwide [2], but are associated with large socioeconomic burdens [5]. Direct lifetime costs can rise to 2.3 million US$ for individuals injured at the age of 25 in the USA [2]. As highlighted in injury prevention models [6, 7], biomechanical investigations are lacking but essential to inform the understanding of the underlying injury mechanisms during dynamic neck loading, and develop effective injury prevention strategies.

The importance of neck muscle activation strategies, and the resulting muscle forces, during the analysis of cervical spine injury mechanisms has been described by both experimental [8, 9] and computational [10, 11] studies. Neck muscles not only mobilise the head and cervical spine, but also alter intervertebral joint loading [12]. Experimental *in vitro* studies have underlined the importance of replicating neck muscle forces as these can alter load transmission across intervertebral joints [9] and the failure load [13] of the cervical spine. Similarly, the inclusion of muscle forces in numerical simulations of the neck affects both intervertebral loading [11] and the resulting kinematics [14, 15] caused by impacts. These studies provide a strong rationale for considering muscles contribution when investigating neck injury mechanisms. However, due to experimental and ethical limitations, little is known about how neck muscles are activated *in vivo* before impacts. This lack of knowledge has led to computational studies applying arbitrary muscle activations or forces during simulations or defining a priori objective criteria to estimate muscle forces through optimisation strategies [10, 11, 15] [16]. This is an important consideration as understanding how muscles are activated prior to impacts is critical to fully inform future neck injury mechanism research and to design preventative measures.

Electromyography (EMG) is therefore an important method to inform numerical simulations and generate more plausible muscle activations that do not fully rely on mathematical a priori criteria. For this reason, surface EMGs have been successfully integrated in simulations of gait [17–19], and upper limb movements [16] to provide realistic estimation of net joint moments and contact forces. However, this approach becomes much more challenging when applied to trunk and neck segments due to the architecture and anatomical overlap of spinal muscles. Fine-wire electromyography provides a potential solution to avoid cross-talk and reach deep spinal muscles, and it has been used to investigate static and quasi-static neck movement tasks [12, 20]. However, the invasive nature of this measurement technique has so far limited investigations of dynamic movements (e.g. collisions) to highly controlled conditions [21, 22]. Furthermore the use of fine-wire EMGs on the neck region during dynamic sporting events is even more limiting due to ethical and experimental constraints (i.e. invasiveness and interference with task performance). Therefore, a combination of experimentally viable and computationally valid methods is currently the only practical strategy to better estimate neck muscle activations and resulting net joint moments during dynamic events.

In neuromusculoskeletal modelling, EMG-assisted methods combine experimental EMG signals with optimisation procedures to generate muscle activation patterns that track both experimental muscle EMG signals and joint moments [23–25]. In previous studies these methods have been applied successfully to the hip [18], knee [19] and shoulder [16] as well as to single intervertebral joint levels (e.g. C4-C5 or L5-Sacrum) of the spine region during static and functional tasks [23, 26–29]. However, the use of EMG-assisted methods to generate intervertebral joint equilibrium across the entire cervical spine (Skull-C1 to C6-C7) during dynamic tasks, representative of contact sports associated with traumatic neck injuries, have not been investigated. Importantly, EMG-assisted methods, to a certain extent, can circumvent the challenge of defining appropriate a priori objective criteria for optimisations adopted by the neuromuscular system during impact events, and assist in the identification of physiologically plausible muscle activation strategies.

Musculoskeletal model estimates of muscle activations and internal loads have been shown to improve with model personalisation [30] whilst other studies have seen no effect [17]. Subject-specific anatomical measurements from magnetic resonance imaging (MRI) can be used to inform region specific scaling [17], individual muscle maximal force production estimates [31] and three-dimensional muscle paths in models [32]. The importance of subject-specific information can be valuable in sporting populations where anatomy is significantly different from the average population.

The aims of this study were twofold. The first aim was to create a calibrated EMG-assisted neuromusculoskeletal model with MRI-informed neck musculoskeletal anatomy. This model would permit the estimation of physiologically plausible neck muscle activations and moments across all intervertebral joints of the cervical spine in rugby impacts. The second aim was to assess the effect of different levels of model personalisation (i.e., muscle maximum isometric force and muscle activation patterns) on the model's ability to generate physiologically plausible results, quantified as the accuracy in reproducing inverse dynamic net joint moments and neck muscle activations. It was hypothesised that increasing model personalisation by using EMG-assisted neural solutions and MRI derived muscle strengths would generate simulated activations that successfully replicated the experimental EMG and net joint moment data, better than neural solutions guided by a priori objective function or only EMG-assisted methods.

2 Materials and Methods

A case study comprising multiple trials on a single rugby athlete was used. A neuromusculoskeletal modelling pipeline was created wherein the ability of the model to reproduce inverse dynamic joint moments and muscle activation patterns was tested. Two neuromuscular solution modalities were assessed: static optimisation and EMG-assisted methods. Additionally, the level of personalisation of the model and its performance was assessed by incorporating

MRI derived muscle maximal isometric force into the model when using the EMG-assisted methods.

2.1 Participant

One professional academy-level front-row rugby player (male, 22 years, 1.82 m, 113.7 kg) participated in this study. Ethical approval was obtained from the Research Ethics Approval Committee for Health of the University of Bath and the participant provided written informed consent prior to data collection.

2.1.1 Medical Imaging

The participant underwent isotropic T1-weighted magnetic resonance imaging (MRI) (Skyra, SIEMENS, Germany) scans of the neck and upper shoulders (occiput to T1 level) with a slice thickness of 1 mm (RT = 7 ms; ET = 2.5 ms). Sequences were taken with the participant in neutral, maximal flexion and maximal extension supine postures. Musculoskeletal structures (skull to C7 vertebrae and muscles) were semi-automatically segmented (Mimics v22, Materialise, Belgium) to scale the musculoskeletal model used in the study. Thirteen bilateral muscle pairs (Figure S1 – Supplementary Material) that were clearly identifiable in the MRI images were segmented by a single operator guided by musculoskeletal atlases [33,34]. Segmented muscle volumes and 3D centroid paths were then derived from the identified muscles using inbuilt algorithms within Mimics v22. Maximal muscle isometric forces (i.e. muscle strengths) were calculated from the segmented muscle volumes based on the relationship proposed by O'Brien et al (2010) [31] (Equation 1):

$$F_{max}^{iso} = \sigma \frac{V^m}{l_0^m} \quad (1)$$

Where sigma is the muscle's specific tension set to 0.55 MPa [31], V^m is the segmented muscle volume (m^3) and l_0^m is the muscle's optimal fibre length (m) from the scaled model [35] subsequently discussed. Further details are presented in the Supplementary Material.

2.1.2 Experimental Methods

To test the performance of the proposed neuromusculoskeletal method in dynamic impact events the participant performed laboratory-based machine rugby scrummaging [36, 37] and tackling [38] trials on the same day as the MRI scans. Neck functional movement in the three cardinal planes of motion (i.e. flexion/extension, left/right lateral bending and left/right axial rotation) against no resistance were also performed. Three successful trials were collected for each dynamic condition (i.e. scrummaging, front and side-on tackling) as a best compromise between representativeness, exposure to multiple impacts and reducing the effects of fatigue. Full body kinematics [35] (Oqus, Qualysis, Sweden) and bilateral EMG (Trigno, Delsys, USA) of the sternocleidomastoid and upper trapezius muscles [35,38] were collected at 250 Hz and 2500 Hz, respectively. The EMG sensors were placed on the muscles belly as explained in the SENIAM (http://www.seniam.org) guidelines. Maximum voluntary isometric contractions (MVIC) were also performed following established methods [39] with the participant in a neutral neck posture performing maximal flexion, extension and lateral neck bending exercises. Due to the large hypertrophy of rugby athletes' neck musculature, radiographically observed by Brauge et al. (2015) [40] and also in this study, only the two major bilateral flexors (*sternocleidomastoids*) and extensors (*trapezius*) could be reliably measured with surface electromyography without crosstalk from other superficial muscles. Additionally, the dynamic nature of the experimental rugby activities involves direct forceful contact with participant's neck area making the use of intra-muscular electrodes considerably challenging and ethically unadvisable due to the risk for the participant. Experimental marker trajectories were low-pass filtered with a fourth-order zero-lag Butterworth filter at 6 Hz in Matlab R2017a (The Mathworks Inc., Natick MA, USA). The EMG signals were band-pass filtered (10-250 Hz; maintaining 97% of signal power), full wave rectified, low-pass filtered at 6 Hz [41] with the same filter, then amplitude normalised to the maximum recorded value identified in the MVIC or dynamic trials prior to impact to create EMG linear envelopes.

2.1.3 Musculoskeletal Modelling

The population specific Rugby Model [35] was updated and used as the baseline model for this study. The hyoid muscle group was added to the Rugby Model to improve its physiological fidelity [42] increasing the number of muscle-tendon units (MTU) that actuated the cervical spine to 96 (64 extensors and 32 flexors). The neck region (C1-C7) of the musculoskeletal model was scaled in each dimension (height, width and depth) in OpenSim 3.3 [43] based on anatomical measurements of the participant's cervical vertebrae from the segmented MRI images. MTU attachment sites were not changed with respect to Vasavada et al. (1998) [44], due to difficulties in identifying muscle attachment locations in the MRI. The remaining model segments were linearly scaled based on anatomical motion capture markers. Six parametric muscle wrapping surfaces (Figure 1) were also defined in the musculoskeletal model to better replicate MTU lines of action in the cervical spine: i) a cylinder anterior to the lower cervical spine registered to the C6 vertebra [45]; ii) a sphere originating and registered to the C2 vertebra; iii) two bilateral cylinders at the posterior of the upper cervical spine also registered to the C2 vertebra; iv) lastly two bilateral tori at the lower cervical spine registered to the C7 vertebra. All wrapping surfaces were constrained to move with their registered bodies. The choice of parameters and position used to define the model's wrapping surfaces were informed by Vasavada et al. (2008) [46] and measurements taken from the segmented MRI images of the rugby player participant. Further details on the wrapping surface definition and registration to their respective MTUs are

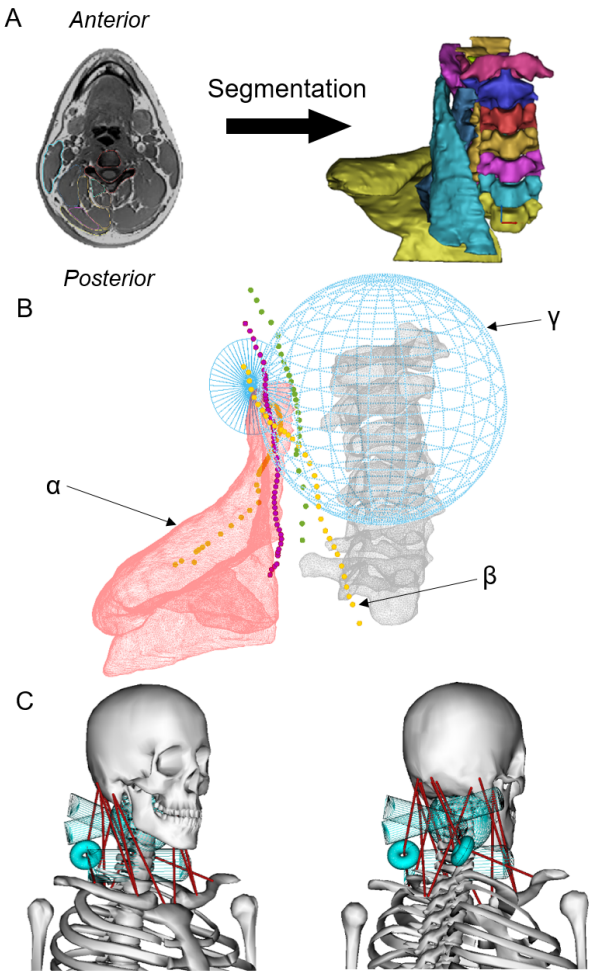

Fig. 1: Representation of the three main steps to update the OpenSim Rugby Model's muscles paths: **A)** high resolution (1 mm isotropic) MRI scans of a rugby forward player's neck and upper-shoulder region were segmented yielding muscle and bone geometries together with muscle volume and centreline information; **B)** musculoskeletal geometries (α) and muscle centroid paths (β) were imported into Matlab and parametric surfaces (γ) were estimated based on [46]; **C)** parameters were used for the generation of wrapping surfaces in the OpenSim model (here only the muscles constrained by the defined wrapping surfaces are presented in the model and the scapulae removed for better visualisation of muscles)

given in the Supplementary Material. The Rugby Model and simulation outputs are available from the SimTK repository (https://simtk.org/projects/csibath).

Functional movement and dynamic rugby trials (500 ms preceding the time of impact) were analysed via three inverse modelling processes: *i)* inverse kinematics, *ii)* inverse dynamics and *iii)* muscle analyses using the OpenSim 3.3 Matlab API. These processes respectively calculated *i)* joint kinematics, *ii)* net joint moments (hence called inverse dynamic joint moments) as well as *iii)* MTU kinematics (length and velocity) and moment arms. As is common during inverse analyses of spine musculoskeletal models [29,35,42,44,47] intervertebral joint angles were driven by coordinate coupler constraints [48]. These constraints partitioned the experimentally measured angle of the head relative to the trunk to the internal coordinates [44] of the cervical spine (i.e. intervertebral joint angles). The constraints were only used during inverse kinematics to obtain intervertebral joint angles. The coordinate coupler constraints were not applied during OpenSim inverse dynamics (ID) and muscle analysis (MA) as they interfere with the estimation of ID joint moments and MTU kinematics in OpenSim. In order to complete ID and MA in OpenSim the musculuskeletal model's coordinate values were prescribed to those computed in the previous IK step. No reserve actuators were included in the model which allowed for the intervertebral joints to be purely actuated by the model's MTUs.

2.1.4 Neuromuscular modelling

The estimation of the model's 96 muscle activation patterns was solved using the Calibrated EMG-Informed Neuromusculoskeletal Modelling (CEINMS) OpenSim Toolbox [24,25] that minimised the following cost function (Equation 2):

$$F = \alpha E_M + \beta E_{\sum e^2} + \gamma E_e \quad (2)$$

Where E_M was the sum of the squared differences between the estimated and inverse dynamic net joint moments from the inverse dynamics (sagittal and frontal plane moments of the C0-C1 through to C6-C7 joints), $E_\Sigma e^2$ was the sum of the squared synthesised activations for all MTUs, and E_e was the sum of the differences between the adjusted model activations and experimental activations. Factors α, $\beta$and γwere non-negative weightings for each term of the cost function. Activation dynamics were characterised by a critically damped linear second-order differential system [24,41]. It was assumed that the MTU tendons of the model were stiff due to their short length and function in the neck. Three neural solution methodologies were assessed in their ability to track inverse dynamic neck net joint moments and EMG activation signals of the experimental trials (Figure 2). The features leading to increasing personalisation of the model are summarised in Table 1:

1. *Static optimisation (SO)*: an uncalibrated model was used through a static optimisation algorithm to estimate muscle activation patterns by minimising both the net joint moments errors and the sum of activations squared;
2. *EMG-assisted (EMGa)*: a calibrated model was used along with an EMG-assisted approach to estimate muscle activation patterns;
3. *MRI-informed EMG-assisted (EMGaMRI)*: EMG-assisted approach was used to estimate muscle activation patterns and included MRI derived F^{iso}_{max} values within the calibration;

Table 1: Summary of features used in each of the three neuromusculoskeletal modelling approaches. The ✔indicates inclusion whilst the ✗exclusion of the feature in the specific approach.

Neuromusculoskeletal model features	SO	EMGa	EMGaMRI
MRI informed neck scaling	✔	✔	✔
MRI informed neck muscle wrapping	✔	✔	✔
Calibration	✗	✔	✔
EMG constrained MTU activation estimation	✗	✔	✔
MRI informed neck muscle strengths F^{iso}_{max}	✗	✗	✔

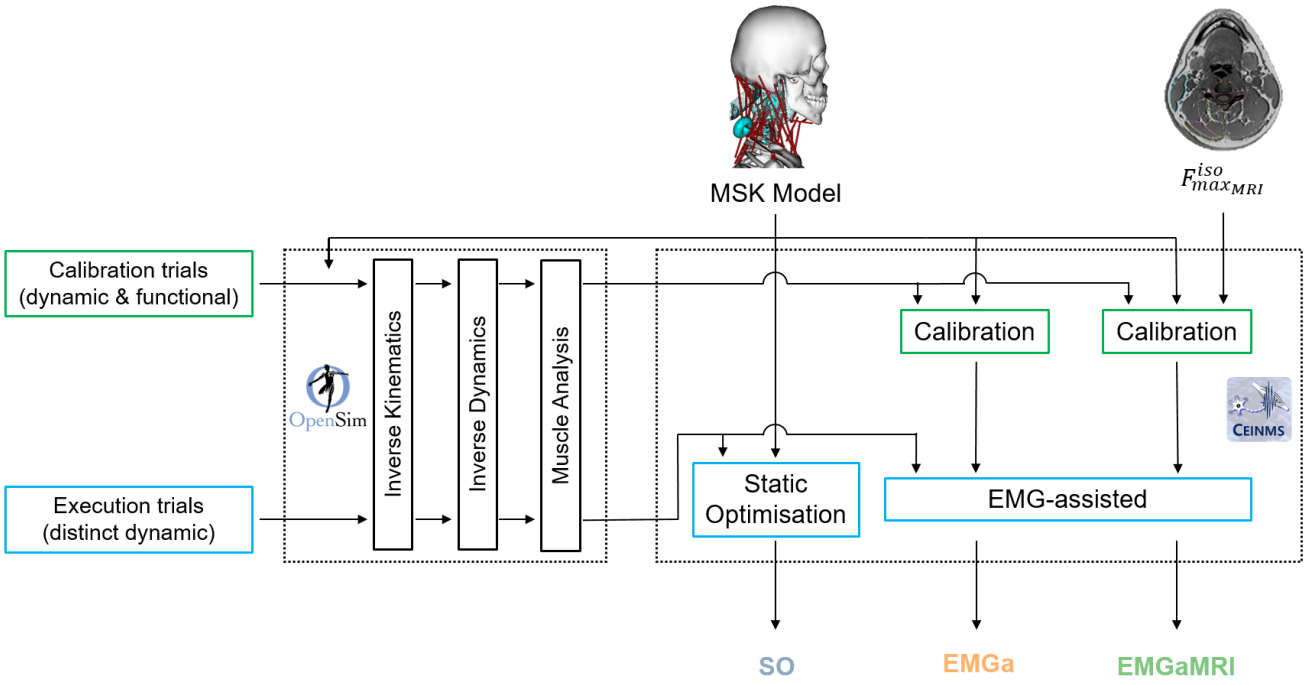

Fig. 2: Schematic overview of computational pipeline used in the study. The scaled musculoskeletal model was used in the analysis of calibration and execution trials with Inverse Kinematic (IK), Inverse Dynamic (ID) and Muscle Analysis (MA) in OpenSim 3.3. The outputs of these analyses (IK: model coordinate kinematics; ID: model coordinate moments; MA: model MTU length, velocity and moment arms) were then used in the CEINMS framework for all Static Optimisation (SO) and EMG-assisted (EMGa and EMGaMRI) neural solutions. For both the EMG-assisted solutions the model underwent the same calibration procedures with the exception of the EMGaMRI that derived muscle maximal isometric forces from the segmentation of muscles identifiable in the MRI. Calibration was completed on a set of dynamic and functional trials that was distinct from the execution trials (tackling and scrummaging) that were analysed with the three neural solutions

2.1.5 Calibration

Calibration in CEINMS was completed through an EMG-driven procedure, where experimental muscle activations (i.e. EMG linear envelopes) were prescribed to the model's MTUs that generate moments about the cervical joints for a set of calibration trials [24]. Musculotendon and activation dynamic parameters [24, 41] were optimised within chosen physiological bounds (Table 2) by minimising the sum of squared differences normalised to trial variance between the predicted and the experimentally measured joint moments for all analysed degrees of freedom (DoF) across the calibration trials [24]. Calibrated musculotendon parameters included tendon slack length (l^t_s), optimal fibre length (l^m_0), a strength coefficient to scale the F^{iso}_{max} of the MTU whilst activation dynamics parameters were two recursive coefficients (C_1 and C_2) and a non-linear shape factor (A) [24, 41].

Table 2: Neuromuscular parameters optimised in CEINMS calibration stage. For detailed explanation on these musculotendon and activation dynamics parameters refer to Lloyd and Besier [41] and Pizzolato et al. [24]

. * Indicates the range was relative to the model's initial parameter value

Parameter	Range
C_1	[-0.95 0.05]
C_2	[-0.95 0.05]
Shape Factor (A)	(-3 0)
Tendon Slack Length (l_s^t)	[0.8 1.2]*
Optimal Fibre Length (l_0^m)	[0.8 1.2]*
Strength Coefficient	[0.6 2.6]*

2.1.6 Calibration Stages

To overcome the high level of redundancy present in the model's neck region, the model underwent two calibrations (intermediate and final) in a three-stage process in CEINMS (Figure 3). This allowed for an intermediate stage where unknown MTU activations could be estimated using the four available EMG linear envelopes. Two functional movement trials (flexion/extension and left/right lateral bending), one scrummaging and one tackling trial were selected for the calibration process. This combination of movements was considered to mobilise the model through a sufficient range of motion. Only the 14 DoF's corresponding to flexion/extension and left/right lateral bending of the intervertebral neck joints were considered when minimising the error between inverse dynamic and estimated net joint moments. The three stages of the calibration process (Figure 3) for the EMGa and EMGaMRI were:

1. *Stage 1* calibrated neuromuscular parameters (Table 2) of the model resulting in an intermediate calibrated model. Initially the 96 MTUs of the uncalibrated musculoskeletal model were separated into functional quadrants (right/left flexion, right/left extension) (Figure 4). Each of the four filtered EMG signals (right/left sternocleidomastoid, right/left upper trapezius) was mapped to all the MTUs of its respective functional quadrant (Table S1). The MTUs were prescribed to follow the mapped EMG signal which assumed MTUs of each functional quadrant were activated identically to the experimental activation signals. For the EMGa solution, the strength coefficient of all MTUs ranged between the minimum (60%) and maximum (260%) differences identified between the MRI derived and baseline model F_{max}^{iso} values (Supplementary material). Whereas for the EMGaMRI solution, the F_{max}^{iso} of the 44 MTUs that constituted the 26 segmented muscles (Table S1) were defined to the MRI derived values. The strength coefficients of these 44 MTUs were set equal to 1 and not varied during the calibration process. The strength coefficients of the remaining MTUs could range between 60 and 260%.
2. *Stage 2* estimated the 86 unknown muscle activations of the calibration trials using the intermediate calibrated model. For each trial the MTUs were again separated into functional quadrants and mapped with their respective experimental EMG signals as in Stage 1. However, this differed to Stage 1 by only constraining activation signals to the flexion (n=6) and extension (n=4) MTUs corresponding to measured muscle EMGs (Table S1). The remaining 86 unknown MTU activations were estimated by adjusting their mapped EMG signal through the CEINMS optimisation that matched inverse dynamic joint moments and minimised deviation from experimental (input) EMG signals.
3. *Stage 3* calibrated the intermediate model's parameters by mapping and constraining each MTU with activation signals. In Stage 3 input activation signals of all model MTUs were mapped from either measured activations, again constrained to the ten corresponding MTUs (as in Stage 1), or individual estimated activations (from Stage 2), constrained to the remaining 86 MTUs in the EMG-driven calibration.

2.2 Data Analysis

Experimental trials (distinct from the calibration trials) were analysed with the SO method by setting the CEINMS weighting factors of Equation 2 to α=1, β=1 and γ=0. This equally weighed the tracking of estimated intervertebral joint moments (α=1) and the minimisation of the activations squared term (β=1) whilst neglecting the estimation of muscle activations from experimental EMG measurements (γ=0). For EMGa and EMGaMRI methods, the activations squared term was neglected (β=0) and the measured activations tracking term engaged (γ>0). For these EMG-assisted methods, the simulated muscle activations were either constrained (N=10) to or adjusted (N=86) whilst tracking their respective experimental EMG linear envelopes (Table 4) in order to minimise errors between inverse dynamic and simulated intervertebral joint moments. Constraining beta (β=0) is acceptable in such cases as the simulated activations are actually following an experimental constraint (i.e. EMG linear envelopes) nonetheless.The $\alpha$and γfactor values were therefore optimised to balance the error between the minimisation of tracking inverse dynamic joint moments and EMG linear envelopes [25], and then slightly adjusted to increase weighting on moment tracking (α=50 and γ=50). To evaluate the performance and the level of physiological agreement of the three neural solutions (SO, EMGa and EMGaMRI), inverse dynamic and simulated net joint moments and muscle activations of each trial were compared using the average root mean squared error (RMSE) (Equation 3) and coefficient of determination (R^2) (Equation 4) across the 500 ms analysis period. Net joint moments RMSE were normalised (NRMSE) to the range of their respective inverse dynamic

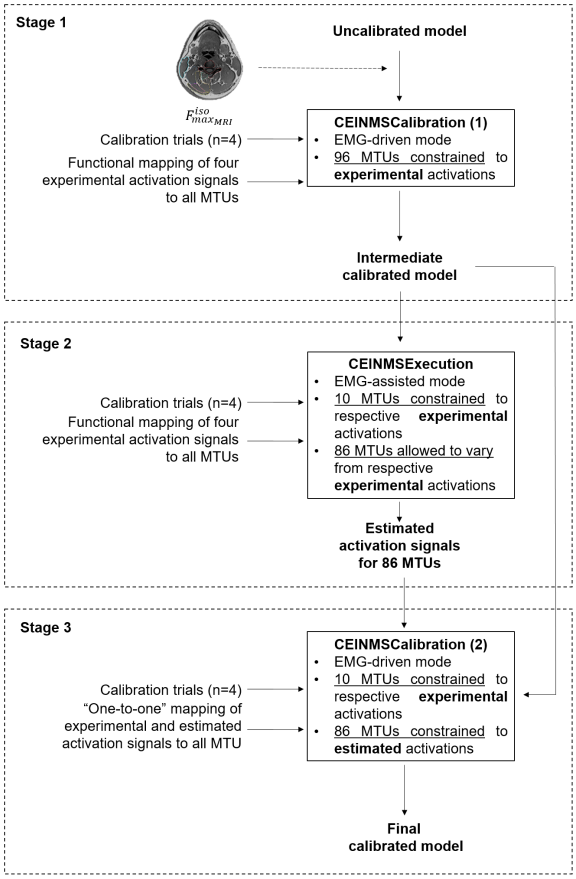

Fig. 3: Flowchart showing the inputs and resulting outputs for the three stage calibration process used for the EMGa and EMGaMRI solutions. For both EMGa and EMGaMRI the calibration procedure was the same apart from EMGaMRI where in Stage 1 $F^{iso}_{max_{MRI}}$ of the model's MTUs (n=44) were updated from segmented muscles volumes (n=26). Detailed information regarding the mapping of experimental activations to MTUs can by sound in Table S2 of the supplementary material

joint moment as the magnitude of moments increased from C0-C1 to C6-C7 (Equation 5).

$$RMSE = \sqrt{\frac{\sum_{i=1}^{N}(x_i^{exp} - x_i^{est})^2}{N}} \tag{3}$$

$$R^2 = 1 - \frac{\sum_{i=1}^{N}(x_i^{exp} - x_i^{est})^2}{\sum_{i=1}^{N} x_i^{exp}(x^{exp_i} - \frac{\sum_{i=1}^{N} x_i^{exp}}{N})^2} \tag{4}$$

$$NRMSE = \frac{RMSE}{x_{max}^{exp} - x_{min}^{exp}} x100\% \tag{5}$$

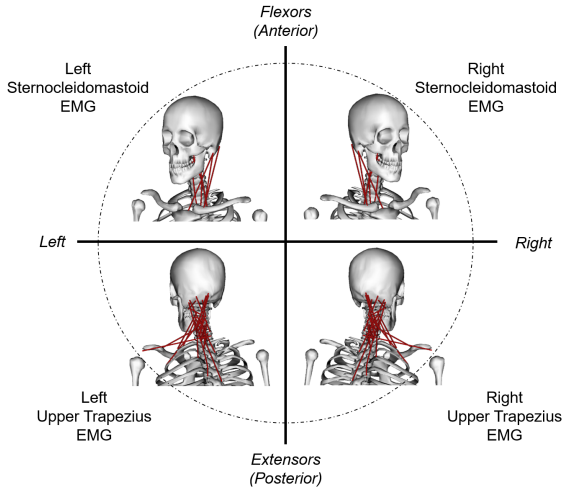

Fig. 4: Representation of how the 96 muscles of the model were separated into functional quadrants of left flexion (16 muscles), right flexion (16 muscles), left extension (32 muscles) and right extension (32 muscles). The separation of the muscles into functional quadrants allowed for the prescription of the experimental EMG signals (right/left sternocleidomastoid, right/left upper trapezius) to the respective functional muscle groups in the EMG-assisted methods

Where x_i^{exp} and x_i^{est} are the experimental and estimated values of the variable under analysis (net joint moment or muscle activation) at the i^{th} time sample of the total N=125 samples (500 ms at 250 Hz). For the normalisation of net joint moment RMSE the x_{max}^{exp} and x_{max}^{est} are the maximum and minimum values of the respective net joint moment under analysis. A one-way analysis of variance (ANOVA) and Tukey-Kramer post-hoc test was performed in Matlab to determine statistically significant differences between the three neural solutions. Significance was set at an alpha value of 0.05. Co-contraction indices [49] of estimated activations were calculated and compared to experimental EMG signals for flexion-extension (Equation 6) and lateral bending (Equation 6). For flexion-extension the activations of the model's flexors (A_f) and extensors (A_e) were separately grouped and averaged then compared to the average flexor (sternocleidomastoids) and extensor (upper trapezius muscles) EMG. Similarly for lateral bending left (A_{Llb}) and right (A_{Rlb}) lateral bending activation averages were calculated and compared respectively to the left (*sternocleidomastoid* and *upper trapezius*) and right (*sternocleidomastoid* and *upper trapezius*) EMG signals:

$$CCI_{FE} = \begin{cases} 1 - \frac{A_f}{A_e}, & A_f < A_e \\ \frac{A_e}{A_f} - 1, & A_e \leqslant A_f \end{cases}$$

$$CCI_{LB} = \begin{cases} 1 - \frac{A_{Llb}}{A_{Rib}}, & A_{Llb} < A_{Rrb} \\ \frac{A_{Rib}}{A_{Llb}} - 1, & A_{Rrb} \leqslant A_{Llb} \end{cases} \tag{6}$$

These ratios provide the relative amount of muscle co-contraction for flexion-extension and lateral bending across the whole cervical spine. A value near 0 represents higher levels of co-contraction, near 1 is higher extension or right lateral bending and near -1 higher flexion or left lateral bending activations.

3 Results

The average net joint moment RMSE across all trials and joint levels showed that EMGaMRI (RMSE = 0.95 $\pm$ 0.74 Nm; R^2 = 0.95 $\pm$ 0.12) neuromuscular solutions tracked experimental flexion/extension net joint moments more accurately than SO (RMSE = 2.32 $\pm$ 1.82 Nm; R^2 = 0.87 $\pm$ 0.22) and EMGa (RMSE = 1.14 $\pm$ 1.04 Nm; R^2 = 0.84 $\pm$ 0.29) (Figure 5). Both RMSE and NRMSE of EMGaMRI and EMGa were significantly ($p \leq 0.01$) lower than SO whilst R^2 only showed significant differences between the two EMG-assisted solutions (Table 3). In lateral bending SO (RMSE = 0.84 $\pm$ 0.59 Nm; R^2 = 0.89 $\pm$ 0.17) had lower RMSE than EMGaMRI (RMSE = 1.07 $\pm$ 0.89 Nm; R^2 = 0.90 $\pm$ 0.12) with EMGa showing the largest errors (RMSE = 2.07 $\pm$ 1.37 Nm; R^2 = 0.67 $\pm$ 0.35) (Figure 6). For lateral bending EMGa RMSE and R^2 results were significantly ($p<0.01$) less accurate than SO whilst EMGaMRI showed no significant difference from SO. Both RMSE and NRMSE and R^2 values showed net joint moments in the upper cervical spine region (C0-C1 through to C3-C4 level) were not tracked as well as the lower cervical spine (C4-C5 through to C6-C7) for all methods (Supplementary material).

Tracking of experimental activations for the ten MTUs corresponding to the four measured muscles was significantly (p¡0.01) better with EMGa (RMSE = 0.04 $\pm$ 0.02; R^2 = 0.89 $\pm$ 0.08) and EMGaMRI (RMSE = 0.03 $\pm$ 0.02; R^2 = 0.92 $\pm$ 0.06) than SO (RMSE = 0.36 $\pm$ 0.22; R^2 = 0.14 $\pm$ 0.20) (Figure 7). The activations of the remaining 86 MTUs maintained a similar pattern to the initial prescribed signals (Figure 8). In contrast SO was not able to reproduce the experimental signal patterns across MTUs with low R^2 average values (Figure 7).

There were clear differences in the MTU recruitment patterns between the SO and the two EMG-assisted solutions (Figure 8). The SO solution created high frequency transitions in activation levels with distinguishable "on-off" phases and frequent saturation. The estimates from the two EMG-assisted solutions showed muscle activations followed the pattern of experimental EMG input signals with individual muscle groups (e.g. *multifidus*, *erector spinae*) varying the signal for their constituent MTUs. This resulted in a closer approximation of experimental co-contractions nearer to the time of impact in both flexion-extension and lateral bending.

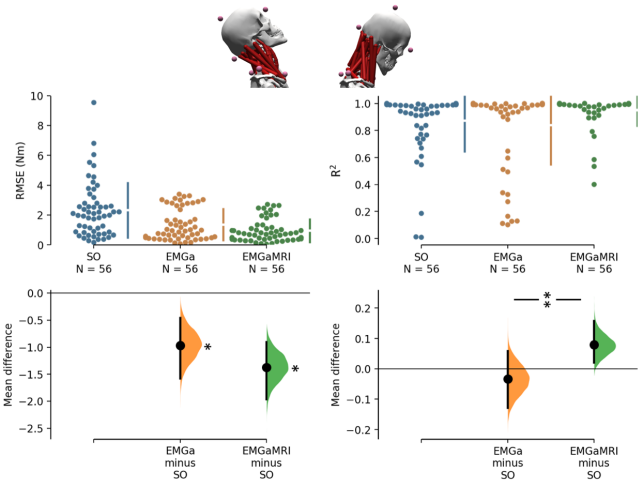

Fig. 5: *FLEXION - EXTENSION* - RMSE (left) and R^2 (right) from the neuromusculoskeletal model with different neural solutions tracking inverse dynamics (ID) flexion/extension net joint moments across different joints and trials. The RMSE and R^2 values are the average across the 500 ms analysis period for each trial and joint level. These are shown in Cumming plots that present above the individual (solid marker), mean (gap between the vertical error bars) and standard deviation (vertical error bars) performance for SO (blue), EMGa (orange) and EMGaMRI (green) solutions. A total number of N = 56 data points corresponds to each of the seven (7) joint levels for each of the eight (8) trials. Below the mean difference and data distribution about the mean of the two EMG-assisted neural solutions (EMGa and EMGaMRI) from the SO solution is presented. Statistically significant difference of each EMG-assisted solution from the SO solution is shown by a single asterisk whilst significance between the two EMG-assisted solutions is indicated by a double asterisk

4 Discussion

In this study we showed that physiologically plausible net joint moments of the cervical spine and neck muscle activations during dynamic neck motions can be predicted by personalised EMG-assisted neuromusculoskeletal models. Rugby impact activities (i.e. tackling and scrummaging) were chosen as a case study and a combination of experimental and modelling approaches were adopted to provide physiological and reliable estimation of neck muscle activation patterns during impact events. A musculoskeletal model of a rugby forward player was created and its ability to generate required neck joint moments was assessed through three neural solutions with increasing levels of subject-specificity. For the first time, we demonstrated that an MRI-informed EMG-assisted solution can generate neck muscle activations that closely match experimental activations, and replicate the required mechanical demands (i.e. net joint moments) of an impact event across the entire cervical spine.

The pure optimisation method (SO) accurately tracked net joint moments, but poorly replicated physiological muscle activation patterns from the experimental trials (Figures 5-8). Poor replication of physiologic muscle activation patterns by SO is likely caused by the large muscle redundancy in the neck and that SO formulations are usually not constrained to experimental EMG measurements but only to a priori objective criteria. In fact, the assumption of a priori

Table 3: Statistical significance of the difference between the three neural solutions for flexion/extension, lateral bending and muscle activations. Each of the three metrics of root mean squared error (RMSE) normalised root mean squared error (NRMSE) and coefficient of determination (R^2) was tested for significance. Statistical significance was determined by a one-way ANOVA and a Tukey-Kramer post-hoc test. Significant differences were set at an alpha level of 0.05

p-values	Flexion / Extension			Lateral Bending			Activations	
Model	RMSE	NRMSE	R^2	RMSE	NRMSE	R^2	RMSE	R^2
SO - EMGa	0.0002	0.0100	0.7019	0.0001	0.0000	0.0001	0.0001	0.0001
SO - EMGaMRI	0.0001	0.0001	0.1469	0.4524	0.9118	0.9768	0.0001	0.0001
EMGa - EMGaMRI	0.2195	0.2895	0.0205	0.0001	0.0001	0.0001	0.9735	0.4621

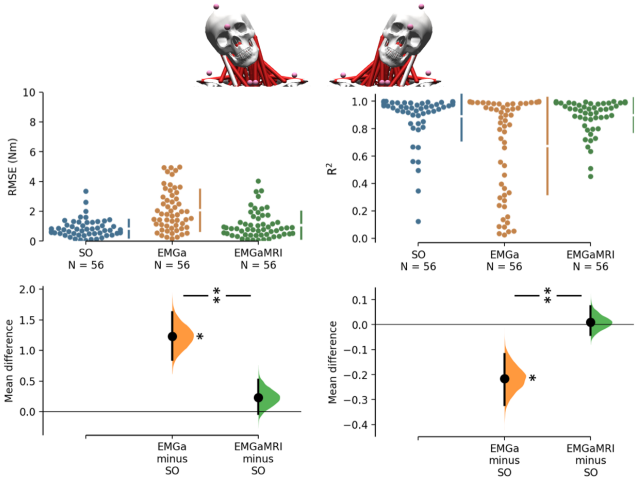

Fig. 6: *LATERAL BENDING* - RMSE (left) and R^2 (right) from the neuromusculoskeletal model with different neural solutions tracking inverse dynamics (ID) lateral bending net joint moments across different joints and trials. The RMSE and R^2 values are the average across the 500 ms analysis period for each trial and joint level. These are shown in Cumming plots that present above the individual (solid marker), mean (gap between the vertical error bars) and standard deviation (vertical error bars) performance for SO (blue), EMGa (orange) and EMGaMRI (green) solutions. A total number of N = 56 data points corresponds to each of the seven (7) joint levels for each of the eight (8) trials. Below the mean difference and data distribution about the mean of the two EMG-assisted neural solutions (EMGa and EMGaMRI) from the SO solution is presented. Statistically significant difference of each EMG-assisted solution from the SO solution is shown by a single asterisk whilst significance between the two EMG-assisted solutions is indicated by a double asterisk

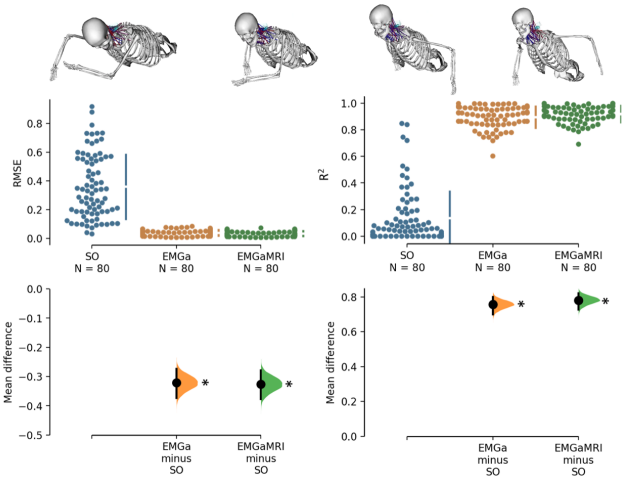

Fig. 7: *MUSCLE ACTIVATIONS* - RMSE (left) and R^2 (right) of neck different neural solutions when tracking experimental EMG signals (right trapezius, left trapezius, right sternocleidomastoid, left sternocleidomastoid) across different trials. The RMSE and R^2 values are the average across the 500 ms analysis period for each trial. These are shown in Cumming plots that present above the individual (solid marker), mean (gap between the vertical error bars) and standard deviation (vertical error bars) performance for SO (blue), EMGa (orange) and EMGaMRI (green) solutions. A total number of N = 80 data points corresponds to each of the ten (10) corresponding MTUs for each of the eight (8) trials. Below the mean difference and data distribution about the mean of the two EMG-assisted neural solutions (EMGa and EMGaMRI) from the SO solution is presented. Statistically significant difference of each EMG-assisted solution from the SO solution is shown by a single asterisk

criteria in objective functions used to guide the estimation of neck muscle activations may not be an accurate approach, due to our current lack of understanding of neck muscle recruitment in preparation for sporting and other impacts. Mortensen et al. (2018) [15] illustrated that metabolic and mechanical static optimisation objective functions produced different neck kinematics under the effect of gravity. The objective criteria used in that study maximised either joint stiffness or joint moment generation capacity which resulted in the smallest neck angle displacement. Although this may

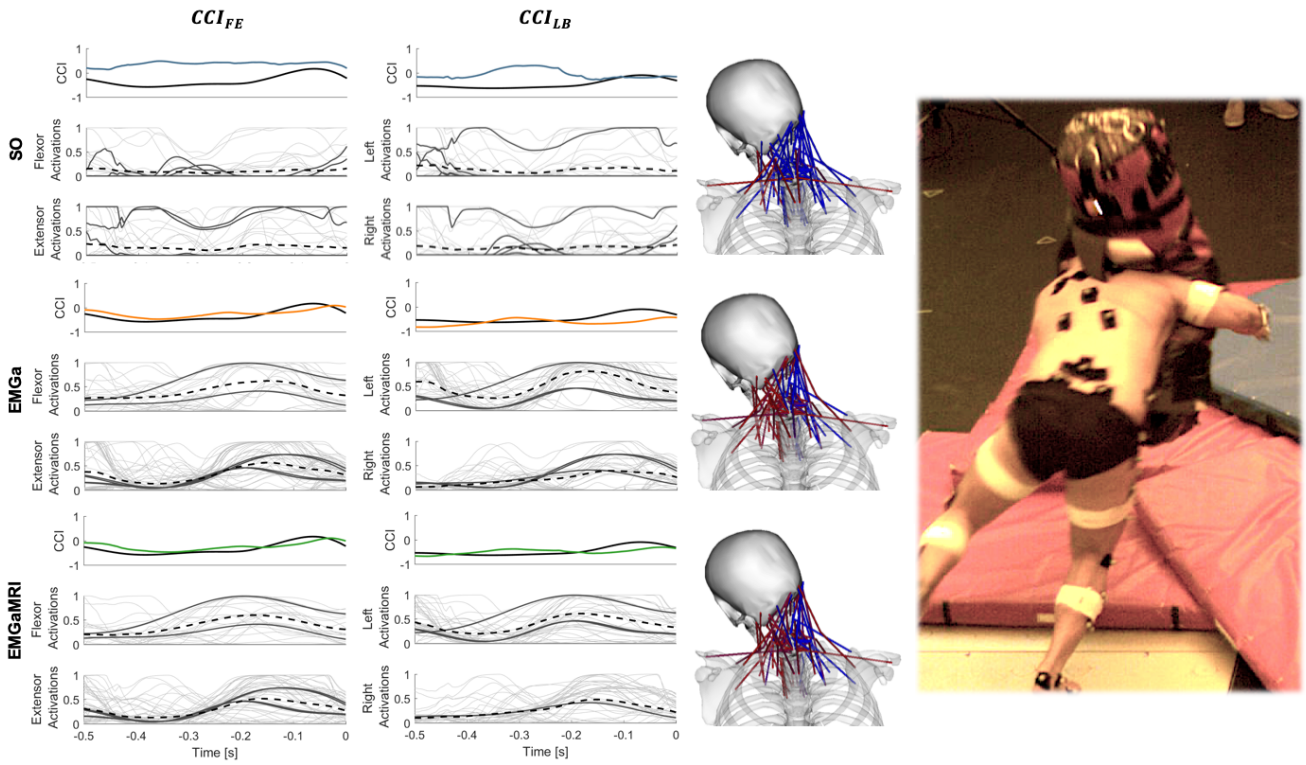

Fig. 8: Left: mean of 5 tackling trials' co-contraction index (CCI_{FE} and CCI_{LB}) of the four experimental EMG signals (solid black) and estimated for SO (top - blue), EMGa (middle – orange) and EMGaMRI (bottom – green) for the 500 ms before impact. Subplots show the muscle group activations used to calculate the estimated CCI values during an individual tackling trial (flexors and extensors CCI_{FE}; left and right lateral flexors for CCI_{LB}). The 86 MTUs that had no measured experimental EMG and were either synthesised (SO) or adjusted (EMGa and EMGaMRI) from their input signal (mapped from the left and right sternocleidomastoid and upper trapezius muscles EMG) are shown in grey, the 10 for which experimental EMG was measured (constrained to the left and right sternocleidomastoid and upper trapezius muscles) in solid black and average activations for each muscle group are plotted as dashed lines for each solution. Centre: snapshots of the musculoskeletal model at the point of impact (depicted right) with MTUs coloured to matched the level of estimated activations for each neural solution (red – high; blue – low). Right: still of the experimental set-up with the participant simulating a tackle during EMG and kinematic measurements

be favourable to minimise neck motion, it may not be an optimal method in situations where adequate neck mobility is required to safely position the head in preparation for impact, such as the preparatory phase of rugby tackling (Figure 8). In our study, the use of EMG-assisted solutions successfully tracked inverse dynamic net joint moments whilst concurrently providing physiological estimates of unknown muscle activations. The ability of the EMG-assisted solutions to reproduce two experimental variables (i.e. net joint moments and muscle activations) and reach physiologically acceptable solutions across the cervical spine with no assumption of a priori objectives (metabolic or mechanical) supports the validity of the presented methods during dynamic neck motions. Our study extends these EMG-assisted methods to the entire cervical spine as the results are in line with previous studies investigating the upper [16] and lower [17, 18] limbs as well as a single joint level of the lumbar spine [29].

The additional incorporation of MRI derived neck muscle strengths in the EMGaMRI solution further improved the tracking of inverse dynamic net joint moments especially in the upper cervical spine compared to the EMGa solution (see Appendix). The upper cervical spine region of the model is likely to have performed better due to the increased force generating capacity of the muscles after they were informed by the MRI measurements. The inherent limitation of accurately modelling the morphology of the spinal musculature in musculoskeletal models. Assigning accurate muscle strength values for the set of 44 MTUs in EMGaMRI illustrates the importance of future detailed models describing the complexity of the neck region. The incorporation of personalised musculoskeletal information with EMG-assisted neural solutions was shown to improve tracking of net moments and experimental activations in the lower limbs of children [17]. This may suggest that in populations where musculoskeletal characteristics (e.g. strength and anatomy) are significantly different than the average populations, such as rugby athletes [40] and children [17], personalised models used for investigations can improve the accuracy internal joint load estimation [19].

This is the first time that neuro-musculoskeletal mod-

els have been able to concurrently match inverse dynamic moment equilibrium across all cervical spine joints (C0-C1 to C6-C7) for dynamic neck motions whilst correctly estimating physiological neck muscle activations. This is a substantial advancement over previous studies that solved for moments across a single cervical joint level [26, 27, 29, 50]. Solving moment equilibrium across all cervical spine levels is important as many major spinal muscles are multi-articulate (span multiple joint levels), and apply loads to multiple cervical joint levels. This approach has also been supported in the lumbar region [51]. Characterisation of the entire cervical spine's internal loading caused by muscle forces is paramount in injury mechanism analysis during dynamic events (e.g. inertial loading or direct impacts) [11, 13]. Muscle forces significantly influence the preloading of intervertebral joints and the propagation of external impact forces down the spinal levels which have already been highlighted in the literature [10, 11, 52]. Future studies that include fine-wire EMG measurements of deep neck muscles with volunteer automotive roll-over simulations [12, 53] would be complemented by our neuro-musculoskeletal modelling technique. With the addition of this modelling technique, a more complete understanding of pre-impact neck dynamics can be obtained compared to the mostly kinematics based previous investigations. Complete dynamic pre-impact analysis can provide detailed initial loading conditions for theoretical simulations of neck injury during impacts. Such simulations could then be used to inform injury prevention strategies such as policy and equipment design changes for sporting and automotive accidents to minimise catastrophic neck injuries.

Muscle co-contraction is an important neural strategy used to stabilise spinal joints [20, 27]. We found that the SO did not track the experimental co-contraction indices, whereas the EMG-assisted solutions preserved neck muscle co-contraction by replicating experimental co-contraction indices. This is an important factor for the analysis of spinal injury mechanism as muscle forces highly influence net joint loading [11]. Previous studies have shown that EMG-assisted models replicate muscle co-contractions when assessed against experimental measures [16, 18, 51]. Models that correctly reproduce muscle co-contractions have been shown to produce more physiologically valid estimates of muscle forces and resulting joint loads [54]. Future studies that estimate mechanical co-contraction indices (i.e. normalised to muscles' moment generating capacity or moment arm) instead of muscle activation alone, could also provide better understanding of muscle action across spinal joints. Our findings support the use of EMG-assisted approaches as a starting point to estimate neck muscle function during dynamic tasks of the head and neck until viable experimental methods are identified or computational estimations using a priori cost functions are verified further.

The following limitations of this study should be considered. Firstly, our musculoskeletal model of the cervical spine is still a simplification of the anatomical complexity of the physical system. The addition of wrapping surfaces, updated muscle strengths and region-specific scaling of the cervical vertebrae based on the participant's MRI measurements aimed to address this issue. Future research should focus on defining dynamic muscle path constraints to better represent human neck anatomy in musculoskeletal models. Updated wrapping surfaces in the musculoskeletal model aim to provide physiological muscle forces in neck positions that do not approach extreme ranges of motion. Such ranges of motion are expected during these sporting tasks and before injury occurs however, future studies investigating functional neck motions and post injury kinematics should aim to improve on such dynamic muscle path constraints. The availability of four measured activation signals as inputs for the EMG-assisted analyses, when 96 MTUs were included in the model, required a number of assumptions that may oversimplify the contribution of individual muscles, especially in deep areas. The positive results provided in Moroney et al. (1988) [55], that also grouped neck muscles, along with our findings, suggest that such a grouping method is a viable initial approach given the limitations associated with applied studies of the neck during impacts. Additionally, McGill et al. (1996) [56] have shown that surface EMGs could represent deeper muscle activations within 15% degree of error in the lumbar spine. In our study the muscle activations that were not measured experimentally could be modulated in order to generate the required forces. Similar approaches have been used previously [27, 50, 56] which we deemed as a reasonable approach based on these assumptions. The single subject EMG-assisted analysis provided subject and task specific muscle activation estimates that matched inverse dynamic moments and EMG measures during representative rugby scrummaging and tackles. The estimated activations are not intended to provide a definite characterisation of the recruitment pattern the nervous system adopts during these rugby tasks, but gives an indication of what can be expected based on available experimental data. However, this consideration has not been seen as a major limitation in previous research estimating spinal muscle function [50, 57]. Future studies should aim to improve EMG-assisted estimations of neck muscle activations by including mechanical objective criteria, such as load protection mechanisms [57], based on observations from experimental studies.

In conclusion, this study shows for the first time that both inverse dynamic net joint moments across the entire cervical spine and neck muscle activation patterns during dynamic tasks can be concurrently reproduced using MRI-informed EMG-assisted models. The ability of the EMG-assisted models to reproduce net joint moments with MTU activations that i) track experimental EMG measurements, ii) do not saturate, iii) do not display high frequency activation and deactivation phases, iv) closely follow experimental co-contraction ratios and v) are estimated with no a priori objective function, is a key step forward to investigate cervical spine injury mechanisms during impact events. The results presented here are not intended to provide a definitive answer on how the neck neuromuscular system functions during dynamic tasks as further investigation is needed for these scenarios. They do, however, illustrate that the presented methods better estimate the neuromuscular state of the entire neck

prior to impacts based solely on experimental data (kinetics and muscle activations) compared to previous numerical methods.

5 Conflict of interest statement

No conflicts of interest to declare from the authors

Acknowledgements

The authors would like to thank the Rugby Football Union Injured Player Foundation for funding the PhD scholarship for PS and the University of Bath International Funding Scheme for helping to fund the international collaboration. Also we would like to thank Mrs Aileen Wilson from CRIC for her kindness and patience during the MRI scans.

References

[1] Dennison, C. R., Macri, E. M., and Cripton, P. A., 2012. "Mechanisms of cervical spine injury in rugby union: is it premature to abandon hyperflexion as the main mechanism underpinning injury?". *British Journal of Sports Medicine,* **46**(8), p. 545.

[2] Organization, W. H., and Society, I. S. C., 2013. International perspectives on spinal cord injury. Report 9241564660, World Health Organization and International Spinal Cord Society.

[3] Sekhon, L. H. S., and Fehlings, M. G., 2001. "Epidemiology, demographics, and pathophysiology of acute spinal cord injury". *Spine,* **26**(24S).

[4] , 1989.

[5] Priebe, M. M., Chiodo, A. E., Scelza, W. M., Kirshblum, S. C., Wuermser, L.-A., and Ho, C. H., 2007. "Spinal cord injury medicine. 6. economic and societal issues in spinal cord injury". *Archives of Physical Medicine and Rehabilitation,* **88**(3, Supplement 1), pp. S84–S88.

[6] Bahr, R., and Krosshaug, T., 2005. "Understanding injury mechanisms: a key component of preventing injuries in sport". *British Journal of Sports Medicine,* **39**(6), pp. 324–329.

[7] van Mechelen, W., Hlobil, H., and Kemper, H. C. G., 1992. "Incidence, severity, aetiology and prevention of sports injuries". *Sports Medicine,* **14**(2), pp. 82–99.

[8] Holsgrove, T. P., Cazzola, D., Preatoni, E., Trewartha, G., Miles, A. W., Gill, H. S., and Gheduzzi, S., 2015. "An investigation into axial impacts of the cervical spine using digital image correlation". *The Spine Journal,* **15**(8), pp. 1856–1863.

[9] Nightingale, R. W., McElhaney, J. H., Richardson, W. J., and Myers, B. S., 1996. "Dynamic responses of the head and cervical spine to axial impact loading". *Journal of Biomechanics,* **29**(3), pp. 307–318.

[10] de Bruijn, E., van der Helm, F. C. T., and Happee, R., 2016. "Analysis of isometric cervical strength with a nonlinear musculoskeletal model with 48 degrees of freedom". *Multibody System Dynamics,* **36**(4), pp. 339–362.

[11] Nightingale, R. W., Sganga, J., Cutcliffe, H., and Bass, C. R., 2016. "Impact responses of the cervical spine: A computational study of the effects of muscle activity, torso constraint, and pre-flexion". *J Biomech,* **49**(4), pp. 558–64.

[12] Newell, R. S., Siegmund, G. P., Blouin, J.-S., Street, J., and Cripton, P. A., 2014. "Cervical vertebral realignment when voluntarily adopting a protective neck posture". *Spine,* **39**(15).

[13] Saari, A., Dennison, C. R., Zhu, Q., Nelson, T. S., Morley, P., Oxland, T. R., Cripton, P. A., and Itshayek, E., 2013. "Compressive follower load influences cervical spine kinematics and kinetics during simulated head-first impact in an in vitro model". *Journal of Biomechanical Engineering,* **135**(11), pp. 111003–111003–11.

[14] Dibb, A. T., Cox, C. A., Nightingale, R. W., Luck, J. F., Cutcliffe, H. C., Myers, B. S., Arbogast, K. B., Seacrist, T., and Bass, C. R., 2013. "Importance of muscle activations for biofidelic pediatric neck response in computational models". *Traffic Injury Prevention,* **14**, pp. 116–127.

[15] Mortensen, J., Trkov, M., and Merryweather, A., 2018. "Exploring novel objective functions for simulating muscle coactivation in the neck". *Journal of Biomechanics,* **71**, pp. 127–134.

[16] Kian, A., Pizzolato, C., Halaki, M., Ginn, K., Lloyd, D., Reed, D., and Ackland, D., 2019. "Static optimization underestimates antagonist muscle activity at the glenohumeral joint: a musculoskeletal modeling study". *Journal of Biomechanics*, p. 109348.

[17] Davico, G., Pizzolato, C., Lloyd, D. G., Obst, S. J., Walsh, H. P. J., and Carty, C. P., 2020. "Increasing level of neuromusculoskeletal model personalisation to investigate joint contact forces in cerebral palsy: A twin case study". *Clinical Biomechanics,* **72**, pp. 141–149.

[18] Hoang, H. X., Diamond, L. E., Lloyd, D. G., and Pizzolato, C., 2019. "A calibrated emg-informed neuromusculoskeletal model can appropriately account for muscle co-contraction in the estimation of hip joint contact forces in people with hip osteoarthritis". *Journal of Biomechanics,* **83**, pp. 134–142.

[19] Serrancolí, G., Kinney, A. L., Fregly, B. J., and Font-Llagunes, J. M., 2016. "Neuromusculoskeletal model calibration significantly affects predicted knee contact forces for walking". *Journal of Biomechanical Engineering,* **138**(8).

[20] Blouin, J.-S., Siegmund, G. P., Carpenter, M. G., and Inglis, J. T., 2007. "Neural control of superficial and deep neck muscles in humans". *Journal of Neurophysiology,* **98**(2), pp. 920–928.

[21] Siegmund, G. P., Blouin, J.-S., Brault, J. R., Hedenstierna, S., and Inglis, J. T., 2006. "Electromyography of superficial and deep neck muscles during isometric, voluntary, and reflex contractions". *Journal of Biomechanical Engineering,* **129**(1), pp. 66–77.

[22] Siegmund, G. P., Blouin, J.-S., Carpenter, M. G., Brault, J. R., and Inglis, J. T., 2008. "Are cervical multifidus muscles active during whiplash and startle? an initial experimental study". *BMC Musculoskeletal Disorders,* **9**, pp. 80–80.

[23] Cholewicki, J., and McGill, S. M., 1994. "Emg assisted optimization: A hybrid approach for estimating muscle forces in an indeterminate biomechanical model". *Journal of Biomechanics,* **27**(10), pp. 1287–1289.

[24] Pizzolato, C., Lloyd, D. G., Sartori, M., Ceseracciu, E., Besier, T. F., Fregly, B. J., and Reggiani, M., 2015. "Ceinms: A toolbox to investigate the influence of different neural control solutions on the prediction of muscle excitation and joint moments during dynamic motor tasks". *Journal of Biomechanics,* **48**(14), pp. 3929–3936.

[25] Sartori, M., Farina, D., and Lloyd, D. G., 2014. "Hybrid neuromusculoskeletal modeling to best track joint moments using a balance between muscle excitations derived from electromyograms and optimization". *Journal of Biomechanics,* **47**(15), pp. 3613–3621.

[26] Cheng, C.-H., Chien, A., Hsu, W.-L., Chen, C. P.-C., and Cheng, H.-Y. K., 2016. "Investigation of the differential contributions of superficial and deep muscles on cervical spinal loads with changing head postures". *PLOS ONE,* **11**(3), p. e0150608.

[27] Choi, H., 2003. "Quantitative assessment of co-contraction in cervical musculature". *Medical Engineering & Physics,* **25**(2), pp. 133–140.

[28] Cholewicki, J., McGill, S. M., and Norman, R. W., 1995. "Comparison of muscle forces and joint load from an optimization and emg assisted lumbar spine model: Towards development of a hybrid approach". *Journal of Biomechanics,* **28**(3), pp. 321–331.

[29] Molinaro, D. D., King, A. S., and Young, A. J., 2020. "Biomechanical analysis of common solid waste collection throwing techniques using opensim and an emg-assisted solver". *Journal of Biomechanics*, p. 109704.

[30] Wesseling, M., De Groote, F., Bosmans, L., Bartels, W., Meyer, C., Desloovere, K., and Jonkers, I., 2016. "Subject-specific geometrical detail rather than cost function formulation affects hip loading calculation". *Computer Methods in Biomechanics and Biomedical Engineering,* **19**(14), pp. 1475–1488.

[31] O'Brien, T. D., Reeves, N. D., Baltzopoulos, V., Jones, D. A., and Maganaris, C. N., 2010. "In vivo measurements of muscle specific tension in adults and children". *Experimental Physiology,* **95**(1), pp. 202–210.

[32] Suderman, B. L., and Vasavada, A. N., 2017. "Neck muscle moment arms obtained in-vivo from mri: Effect of curved and straight modeled paths". *Annals of Biomedical Engineering,* **45**(8), pp. 2009–2024.

[33] Au, J., Perriman, D. M., Pickering, M. R., Buirski, G., Smith, P. N., and Webb, A. L., 2016. "Magnetic resonance imaging atlas of the cervical spine musculature". *Clinical Anatomy,* **29**(5), pp. 643–659.

[34] Moeller, T. B., and Reif, E., 2007. *Pocket Atlas of Sectional Anatomy. Computer Tomography and Magnetic Resonance Imaging*, Vol. Volume 3. Spine, Extremities, Joints. Thieme, Germany.

[35] Cazzola, D., Holsgrove, T. P., Preatoni, E., Gill, H. S., and Trewartha, G., 2017. "Cervical spine injuries: A whole-body musculoskeletal model for the analysis of spinal loading". *PLoS One,* **12**(1), p. e0169329.

[36] Cazzola, D., Preatoni, E., Stokes, K. A., England, M. E., and Trewartha, G., 2014. "A modified pre-bind engagement process reduces biomechanical loading on front row players during scrummaging: a cross-sectional study of 11 elite teams". *British Journal of Sports Medicine*.

[37] Preatoni, E., Cazzola, D., Stokes, K. A., England, M., and Trewartha, G., 2015. "Pre-binding prior to full engagement improves loading conditions for front-row players in contested rugby union scrums". *Scandinavian Journal of Medicine & Science in Sports,* **26**(12), pp. 1398–1407.

[38] Seminati, E., Cazzola, D., Preatoni, E., and Trewartha, G., 2017. "Specific tackling situations affect the biomechanical demands experienced by rugby union players". *Sports Biomechanics,* **16**(1), pp. 58–75.

[39] Cazzola, D., Stone, B., Holsgrove, T. P., Trewartha, G., and Preatoni, E., 2016. "Spinal muscle activity in simulated rugby union scrummaging is affected by different engagement conditions". *Scandinavian Journal of Medicine & Science in Sports,* **26**(1600-0838 (Electronic)).

[40] Brauge, D., Delpierre, C., Adam, P., Sol, J. C., Bernard, P., and Roux, F.-E., 2015. "Clinical and radiological cervical spine evaluation in retired professional rugby players". *Journal of Neurosurgery*(5), p. 551.

[41] Lloyd, D. G., and Besier, T. F., 2003. "An emg-driven musculoskeletal model to estimate muscle forces and knee joint moments in vivo". *Journal of Biomechanics,* **36**(6), pp. 765–776.

[42] Mortensen, J. D., Vasavada, A. N., and Merryweather, A. S., 2018. "The inclusion of hyoid muscles improve moment generating capacity and dynamic simulations in musculoskeletal models of the head and neck". *PLOS ONE,* **13**(6), p. e0199912.

[43] Delp, S. L., Anderson, F. C., Arnold, A. S., Loan, P., Habib, A., John, C. T., Guendelman, E., and Thelen, D. G., 2007. "Opensim: Open-source software to create and analyze dynamic simulations of movement". *IEEE Transactions on Biomedical Engineering,* **54**(11), pp. 1940–1950.

[44] Vasavada, A. N., Li, S. P., and Delp, S. L., 1998. "Influence of muscle morphometry and moment arms on the moment-generating capacity of human neck muscles". *Spine,* **23**(4), pp. 412–422.

[45] Kuo, C., Sheffels, J., Fanton, M., Yu Ina, B., Hamalainen, R., and Camarillo, D., 2019. "Passive cervical spine ligaments provide stability during head impacts". *Journal of The Royal Society Interface,* **16**(154), p. 20190086.

[46] Vasavada, A. N., Lasher, R. A., Meyer, T. E., and Lin, D. C., 2008. "Defining and evaluating wrapping sur-

faces for mri-derived spinal muscle paths". *Journal of Biomechanics,* **41**(7), pp. 1450–1457.

[47] Beaucage-Gauvreau, E., Robertson, W. S. P., Brandon, S. C. E., Fraser, R., Freeman, B. J. C., Graham, R. B., Thewlis, D., and Jones, C. F., 2019. "Validation of an opensim full-body model with detailed lumbar spine for estimating lower lumbar spine loads during symmetric and asymmetric lifting tasks". *Computer Methods in Biomechanics and Biomedical Engineering,* **22**(5), pp. 451–464.

[48] Sherman, M. A., Seth, A., and Delp, S. L., 2013. "Wha is a moment arm? calculating muscle effectiveness in biomechanical models using generalised coordinates.". *Proceedings of the ASME 2013 International Design Engineering Technical Conferences & Computers and Information in Engineering Conference,* **2013**, p. V07BT10A052.

[49] Heiden, T. L., Lloyd, D. G., and Ackland, T. R., 2009. "Knee joint kinematics, kinetics and muscle co-contraction in knee osteoarthritis patient gait". *Clinical Biomechanics,* **24**(10), pp. 833–841.

[50] Arjmand, N., Gagnon, D., Plamondon, A., Shirazi-Adl, A., and Larivière, C., 2010. "A comparative study of two trunk biomechanical models under symmetric and asymmetric loadings". *Journal of Biomechanics,* **43**(3), pp. 485–491.

[51] Gagnon, D., Arjmand, N., Plamondon, A., Shirazi-Adl, A., and Larivière, C., 2011. "An improved multi-joint emg-assisted optimization approach to estimate joint and muscle forces in a musculoskeletal model of the lumbar spine". *Journal of Biomechanics,* **44**(8), pp. 1521–1529.

[52] Nightingale, R. W., Bass, C. R., and Myers, B. S., 2019. "On the relative importance of bending and compression in cervical spine bilateral facet dislocation". *Clinical Biomechanics,* **64**, pp. 90–97.

[53] Newell, R. S., Blouin, J.-S., Street, J., Cripton, P. A., and Siegmund, G. P., 2018. "The neutral posture of the cervical spine is not unique in human subjects". *Journal of Biomechanics,* **80**, pp. 53–62.

[54] Walter, J. P., Kinney, A. L., Banks, S. A., D'Lima, D. D., Besier, T. F., Lloyd, D. G., and Fregly, B. J., 2014. "Muscle synergies may improve optimization prediction of knee contact forces during walking". *Journal of Biomechanical Engineering,* **136**(2).

[55] Moroney, S. P., Schultz, A. B., and Miller, J. A. A., 1988. "Analysis and measurement of neck loads". *Journal of Orthopaedic Research,* **6**(5), pp. 713–720.

[56] McGill, S., Juker, D., and Kropf, P., 1996. "Appropriately placed surface emg electrodes reflect deep muscle activity (psoas, quadratus lumborum, abdominal wall) in the lumbar spine". *Journal of Biomechanics,* **29**(11), pp. 1503–1507.

[57] Van den Abbeele, M., Li, F., Pomero, V., Bonneau, D., Sandoz, B., Laporte, S., and Skalli, W., 2018. "A subject-specific biomechanical control model for the prediction of cervical spine muscle forces". *Clinical Biomechanics,* **51**, pp. 58–66.

[58] Assila, N., Pizzolato, C., Martinez, R., Lloyd, D. G., and Begon, M., 2020. "Emg-assisted algorithm to account for shoulder muscles co-contraction in overhead manual handling". *Applied Sciences,* **10**(10).

[59] Hoang, H. X., Diamond, L. E., Lloyd, D. G., and Pizzolato, C., 2019. "A calibrated emg-informed neuromusculoskeletal model can appropriately account for muscle co-contraction in the estimation of hip joint contact forces in people with hip osteoarthritis". *Journal of Biomechanics,* **83**, pp. 134–142.

[60] Hoang, H. X., Pizzolato, C., Diamond, L. E., and Lloyd, D. G., 2018. "Subject-specific calibration of neuromuscular parameters enables neuromusculoskeletal models to estimate physiologically plausible hip joint contact forces in healthy adults". *Journal of Biomechanics,* **80**, pp. 111–120.

[61] Veerkamp, K., Waterval, N., Geijtenbeek, T., Carty, C., Lloyd, D., Harlaar, J., and van der Krogt, M., 2021. "Evaluating cost function criteria in predicting healthy gait". *Journal of Biomechanics,* **123**, p. 110530.

[62] Diamond, L., Hoang, H., Barrett, R., Loureiro, A., Constantinou, M., Lloyd, D., and Pizzolato, C., 2020. "Individuals with mild-to-moderate hip osteoarthritis walk with lower hip joint contact forces despite higher levels of muscle co-contraction compared to healthy individuals". *Osteoarthritis and Cartilage,* **28**(7), pp. 924–931.

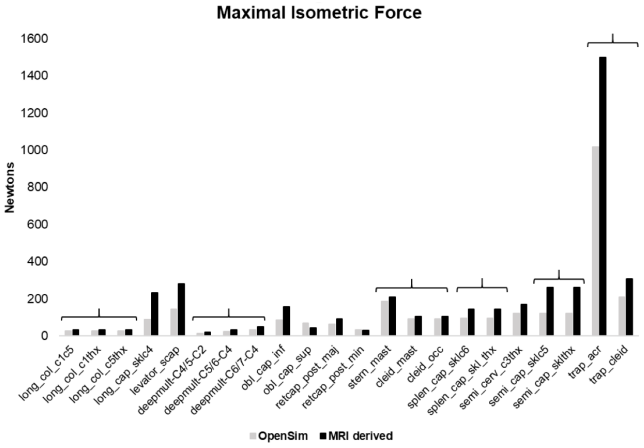

Fig. 9: Changes in model MTU maximal isometric force values (F^{iso}_{max}) informed from segmented muscle volumes. Grey bars represent individual MTU F^{iso}_{max} values and black bars estimated values from MRI information. Multiple MTU under brackets are sub regions of an individual anatomical muscle (e.g. *trap acr* and *trap cleid* are both constituents of the trapezius). Naming of MTUs consistent with OpenSim models

Appendix

Estimation of maximal isometric force and definition of musculoskeletal model wrapping surfaces from MRI measurements

Estimated F^{iso}_{max} derived from the segmented neck muscle volumes ranged between 60 and 260% of the population specific model values [35] with an average increase of 50% (Figure 9) . Only rectus capitis posterior minor and obliquus capitis inferior MRI derived values of F^{iso}_{max} were reduced in relative to the baseline model. The MRI derived estimates of muscle F^{iso}_{max} were separated into their constituent MTU F^{iso}_{max} values relative to the baseline model and updated in the EMGaMRI model. Some sub-regions of the neck musculature, which are defined in the musculoskeletal model as individual muscle-tendon units (MTUs), were not clearly identifiable from the MRI scans, subsequently their F^{iso}_{max} was scaled proportionally to the total F^{iso}_{max} of the original model's MTUs that comprised a whole muscle (Figure 9). Left and right muscle strength was assumed equal in the model thus the average of the MRI derived F^{iso}_{max} values were prescribed to the MTUs.

The parametric wrapping surfaces included in the updated Rugby Model [35] were defined by measurements taken from segmented MRI imaging of muscle and bone structures whilst guided by methods detailed by Vasavada et al. (2008). Initially the raw DICOM image stacks were segmented in Mimics (v22, Materialise, Belgium) providing musculoskeletal geometries (from occiput to base of C7) of the front row rugby player in a neutral supine posture. Volume and centroid path measurements were obtained from the segmented muscles. These data along with the segmented vertebral and skull geometries were then imported into Matlab R2017a (The Mathworks Inc., Natick MA, USA) were the parameters that would define the OpenSim wrapping surfaces could be estimated based on the techniques outlined by Anita N. Vasavada, et al. [46].

The following procedures were followed to include the wrapping surfaces were included in the model:

1. As stated in the main text of the study a single cylinder was defined at the centre of the C6 vertebrae [45]. Other than the identification of the C6 centre of mass the definition of this parametric cylinder was the same as in Kuo et al. (2019) [45].
2. A sphere was created with its origin located at the centre of mass of the C2 vertebrae. Its radius was defined by averaging the shortest distances between the sphere's origin and centroid paths of the left and right sternocleidomastoid muscles' [46].
3. Two cylinders were defined one the left and one on the right posterolateral aspects of the upper vertebral column. Initially the linear path of the of the left and right semispinalis capitis muscles were recreated on the segmented geometries in Matlab by virtually palpating the muscles' insertion on occiput then registering the origin of the muscles to those points from the scaled OpenSim model. This was initially completed because the thoracic region was not visible in the scans and thus could not be virtually palpated in the segmented geometries. After this the nearest semispinalis capitis centroid point to the C2 centre of mass was identified. A perpendicular vector from this location to the linear muscle path vector was then calculated that return the radius (magnitude of vector), centre (location on linear muscle path vector) and orientation (long axis normal to the plane defined by the radius and linear muscle path vectors) of the parametric cylinder. The same was completed on both sides and the mean values were used in the final model to reduce the effect of measurement errors.
4. Two tori were defined one on the left and one on the right posterolateral aspects of the lower cervical spine. Their origins were defined from the trapezius muscle centroid paths. A point of inflection was visually identified and registered to the C7 centre of mass. This was the point where the centroid path progressed from a mostly parallel path with respect to the transverse plane to a perpendicular path. The tori's axes of revolution were aligned with the location of the acromion. The same was completed on both sides and the mean values were used in the final model to reduce the effect of measurement errors.

The estimated parameters from these procedures were then used to define the parametric wrapping surfaces in OpenSim. Once the wrapping surfaces were defined the model was prescribed maximal ranges of motion about single axis and motions combining multiple axes to assess if muscle paths were stable. This was not the case for all surfaces. Manual adjustments in OpenSim were made to the radii and distances of the wrapping surfaces to maintain muscle path stability. During these manual adjustments care was taken to maintain the original orientations and level of the surfaces in

the model.

Mapping of experimental activations to model muscle tendon units in CEINMS

As detailed in the main body of the study muscle activations were either constrained or adjusted from measured EMG linear envelopes depending on their function and if experimental measurements existed (Table 4). This mapping was applied in the CEINMS analysis of execution trials (Figure 12) and in Stage 2 of the calibration process (Figure 13). During Stage 1 and 3 of the calibration process all activations were constrained to their mapped input signals.

Table 4: The 96 muscletendon units (MTUs) used in the model with indication to which functional quadrant they were assigned to, experimental activation signal they received as initial input, if the mapped activation signal was constrained (n=10) or adjusted (n=86) during the solution, if wrapping surfaces constrained the MTUs paths and the 44 MTUs' F^{iso}_{max} were scaled from MRI measurements

Model Muscles	Functional quadrant	Mapped activation input	Designation	Wrapping surface	MRI scaled F^{iso}_{max}
cleid mast	Right flexion	Right Sternocleidomastoid	Constrained	Anterior cylinder, Sphere	TRUE
cleid occ	Right flexion	Right Sternocleidomastoid	Constrained	Anterior cylinder, Sphere	TRUE
stern mast	Right flexion	Right Sternocleidomastoid	Constrained	Anterior cylinder, Sphere	TRUE
long cap sklc4	Right flexion	Right Sternocleidomastoid	Adjusted	N/A	TRUE
long col c1c5	Right flexion	Right Sternocleidomastoid	Adjusted	N/A	TRUE
long col c1thx	Right flexion	Right Sternocleidomastoid	Adjusted	N/A	TRUE
long col c5thx	Right flexion	Right Sternocleidomastoid	Adjusted	N/A	TRUE
scalenus ant	Right flexion	Right Sternocleidomastoid	Adjusted	N/A	FALSE
sterno hyoid	Right flexion	Right Sternocleidomastoid	Adjusted	N/A	FALSE
omo hyoid	Right flexion	Right Sternocleidomastoid	Adjusted	N/A	FALSE
sternothyroid	Right flexion	Right Sternocleidomastoid	Adjusted	N/A	FALSE
digastric post	Right flexion	Right Sternocleidomastoid	Adjusted	N/A	FALSE
digastric ant	Right flexion	Right Sternocleidomastoid	Adjusted	N/A	FALSE
geniohyoid	Right flexion	Right Sternocleidomastoid	Adjusted	N/A	FALSE
mylohyoid post	Right flexion	Right Sternocleidomastoid	Adjusted	N/A	FALSE
mylohyoid ant	Right flexion	Right Sternocleidomastoid	Adjusted	N/A	FALSE
stylohyoid lat	Right flexion	Right Sternocleidomastoid	Adjusted	N/A	FALSE
stylohyoid med	Right flexion	Right Sternocleidomastoid	Adjusted	N/A	FALSE
cleid mast l	Left flexion	Left Sternocleidomastoid	Constrained	Anterior cylinder, Sphere	TRUE
cleid occ l	Left flexion	Left Sternocleidomastoid	Constrained	Anterior cylinder, Sphere	TRUE
stern mast l	Left flexion	Left Sternocleidomastoid	Constrained	Anterior cylinder, Sphere	TRUE
long cap sklc4 l	Left flexion	Left Sternocleidomastoid	Adjusted	N/A	TRUE
long col c1c5 l	Left flexion	Left Sternocleidomastoid	Adjusted	N/A	TRUE
long col c1thx l	Left flexion	Left Sternocleidomastoid	Adjusted	N/A	TRUE
long col c5thx l	Left flexion	Left Sternocleidomastoid	Adjusted	N/A	TRUE
scalenus ant l	Left flexion	Left Sternocleidomastoid	Adjusted	N/A	FALSE
sterno hyoid l	Left flexion	Left Sternocleidomastoid	Adjusted	N/A	FALSE
omo hyoid l	Left flexion	Left Sternocleidomastoid	Adjusted	N/A	FALSE
sternothyroid l	Left flexion	Left Sternocleidomastoid	Adjusted	N/A	FALSE
digastric post l	Left flexion	Left Sternocleidomastoid	Adjusted	N/A	FALSE
digastric ant l	Left flexion	Left Sternocleidomastoid	Adjusted	N/A	FALSE
geniohyoid l	Left flexion	Left Sternocleidomastoid	Adjusted	N/A	FALSE
mylohyoid post l	Left flexion	Left Sternocleidomastoid	Adjusted	N/A	FALSE
mylohyoid ant l	Left flexion	Left Sternocleidomastoid	Adjusted	N/A	FALSE
stylohyoid lat l	Left flexion	Left Sternocleidomastoid	Adjusted	N/A	FALSE
stylohyoid med l	Left flexion	Left Sternocleidomastoid	Adjusted	N/A	FALSE
trap acr	Right extension	Right Upper Trapezius	Constrained	Right torus	TRUE
trap cl	Right extension	Right Upper Trapezius	Constrained	Right torus	TRUE
deepmult-C4/5-C2	Right extension	Right Upper Trapezius	Adjusted	N/A	TRUE
deepmult-C5/6-C3	Right extension	Right Upper Trapezius	Adjusted	N/A	TRUE
deepmult-C6/7-C4	Right extension	Right Upper Trapezius	Adjusted	N/A	TRUE
deepmult-T1-C5	Right extension	Right Upper Trapezius	Adjusted	N/A	FALSE
deepmult-T1-C6	Right extension	Right Upper Trapezius	Adjusted	N/A	FALSE
deepmult-T2-C7	Right extension	Right Upper Trapezius	Adjusted	N/A	FALSE
iliocost cerv c5rib	Right extension	Right Upper Trapezius	Adjusted	N/A	FALSE
longissi cap sklc6	Right extension	Right Upper Trapezius	Adjusted	N/A	FALSE
longissi cerv c4thx	Right extension	Right Upper Trapezius	Adjusted	N/A	FALSE
obl cap inf	Right extension	Right Upper Trapezius	Adjusted	N/A	TRUE
obl cap sup	Right extension	Right Upper Trapezius	Adjusted	N/A	TRUE
rectcap post maj	Right extension	Right Upper Trapezius	Adjusted	N/A	TRUE
rectcap post min	Right extension	Right Upper Trapezius	Adjusted	N/A	TRUE

scalenus med	Right extension	Right Upper Trapezius	Adjusted	N/A	FALSE
scalenus post	Right extension	Right Upper Trapezius	Adjusted	N/A	FALSE
semi cerv c3thx	Right extension	Right Upper Trapezius	Adjusted	N/A	FALSE
supmult-C4/5-C2	Right extension	Right Upper Trapezius	Adjusted	N/A	FALSE
supmult-C5/6-C2	Right extension	Right Upper Trapezius	Adjusted	N/A	FALSE
supmult-C6/7-C2	Right extension	Right Upper Trapezius	Adjusted	N/A	FALSE
supmult-T1-C4	Right extension	Right Upper Trapezius	Adjusted	N/A	FALSE
supmult-T1-C5	Right extension	Right Upper Trapezius	Adjusted	N/A	FALSE
supmult-T2-C6	Right extension	Right Upper Trapezius	Adjusted	N/A	FALSE
semi cap sklc5	Right extension	Right Upper Trapezius	Adjusted	Right posterior cylinder	TRUE
semi cap sklthx	Right extension	Right Upper Trapezius	Adjusted	Right posterior cylinder	TRUE
splen cap sklc6	Right extension	Right Upper Trapezius	Adjusted	Right posterior cylinder	TRUE
splen cap sklthx	Right extension	Right Upper Trapezius	Adjusted	N/A	TRUE
splen cerv c3thx	Right extension	Right Upper Trapezius	Adjusted	N/A	TRUE
levator scap	Right extension	Right Upper Trapezius	Adjusted	N/A	TRUE
trap acr l	Left extension	Left Upper Trapezius	Constrained	Left torus	TRUE
trap cl l	Left extension	Left Upper Trapezius	Constrained	Left torus	TRUE
deepmult-C4/5-C2 l	Left extension	Left Upper Trapezius	Adjusted	N/A	TRUE
deepmult-C5/6-C3 l	Left extension	Left Upper Trapezius	Adjusted	N/A	TRUE
deepmult-C6/7-C4 l	Left extension	Left Upper Trapezius	Adjusted	N/A	TRUE
deepmult-T1-C5 l	Left extension	Left Upper Trapezius	Adjusted	N/A	FALSE
deepmult-T1-C6 l	Left extension	Left Upper Trapezius	Adjusted	N/A	FALSE
deepmult-T2-C7 l	Left extension	Left Upper Trapezius	Adjusted	N/A	FALSE
iliocost cerv c5rib l	Left extension	Left Upper Trapezius	Adjusted	N/A	FALSE
longissi cap sklc6 l	Left extension	Left Upper Trapezius	Adjusted	N/A	FALSE
longissi cerv c4thx l	Left extension	Left Upper Trapezius	Adjusted	N/A	FALSE
obl cap inf l	Left extension	Left Upper Trapezius	Adjusted	N/A	TRUE
obl cap sup l	Left extension	Left Upper Trapezius	Adjusted	N/A	TRUE
rectcap post maj l	Left extension	Left Upper Trapezius	Adjusted	N/A	TRUE
rectcap post min l	Left extension	Left Upper Trapezius	Adjusted	N/A	TRUE
scalenus med l	Left extension	Left Upper Trapezius	Adjusted	N/A	FALSE
scalenus post l	Left extension	Left Upper Trapezius	Adjusted	N/A	FALSE
semi cerv c3thx l	Left extension	Left Upper Trapezius	Adjusted	N/A	FALSE
supmult-C4/5-C2 l	Left extension	Left Upper Trapezius	Adjusted	N/A	FALSE
supmult-C5/6-C2 l	Left extension	Left Upper Trapezius	Adjusted	N/A	FALSE
supmult-C6/7-C2 l	Left extension	Left Upper Trapezius	Adjusted	N/A	FALSE
supmult-T1-C4 l	Left extension	Left Upper Trapezius	Adjusted	N/A	FALSE
supmult-T1-C5 l	Left extension	Left Upper Trapezius	Adjusted	N/A	FALSE
supmult-T2-C6 l	Left extension	Left Upper Trapezius	Adjusted	N/A	FALSE
semi cap sklc5 l	Left extension	Left Upper Trapezius	Adjusted	Left posterior cylinder	TRUE
semi cap sklthx l	Left extension	Left Upper Trapezius	Adjusted	Left posterior cylinder	TRUE
splen cap sklc6 l	Left extension	Left Upper Trapezius	Adjusted	Left posterior cylinder	TRUE
splen cap sklthx l	Left extension	Left Upper Trapezius	Adjusted	N/A	TRUE
splen cerv c3thx l	Left extension	Left Upper Trapezius	Adjusted	N/A	TRUE
levator scap l	Left extension	Left Upper Trapezius	Adjusted	N/A	TRUE

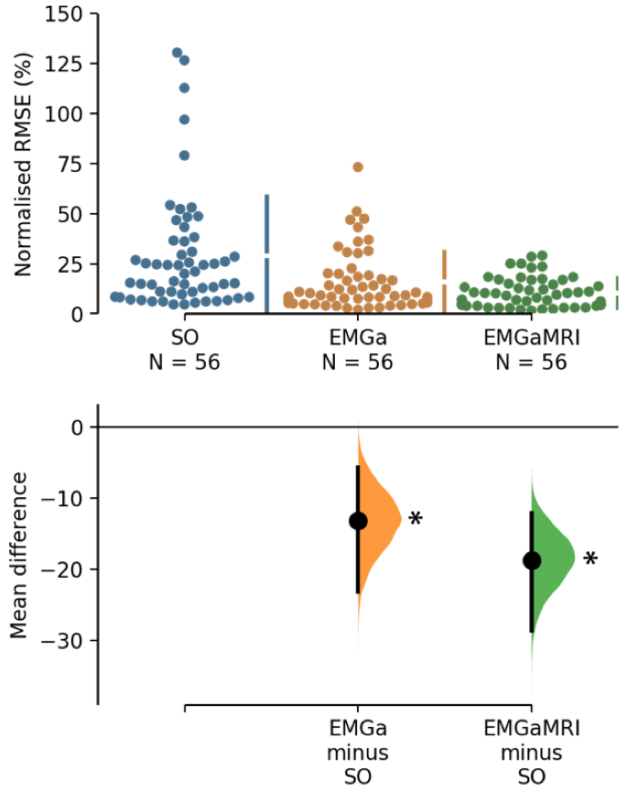

Fig. 10: Pooled normalised RMSE from the neuromusculoskeletal model with different neural solutions tracking inverse dynamics (ID) flexion/extension net joint moments across all joints and trials. The RMSE values are the average across the 500 ms analysis period for each trial and joint level. These are shown in Cumming plots that present above the individual (solid marker), mean (gap between the vertical error bars) and standard deviation (vertical error bars) performance for SO (blue), EMGa (orange) and EMGaMRI (green) solutions. A total number of N = 56 data points corresponds to each of the seven (7) joint levels for each of the eight (8) trials. Below the mean difference and data distribution about the mean of the two EMG-assisted neural solutions (EMGa and EMGaMRI) from the SO solution is presented. Statistically significant difference of each EMG-assisted solution from the SO solution is shown by a single asterisk whilst significance between the two EMG-assisted solutions is indicated by a double asterisk

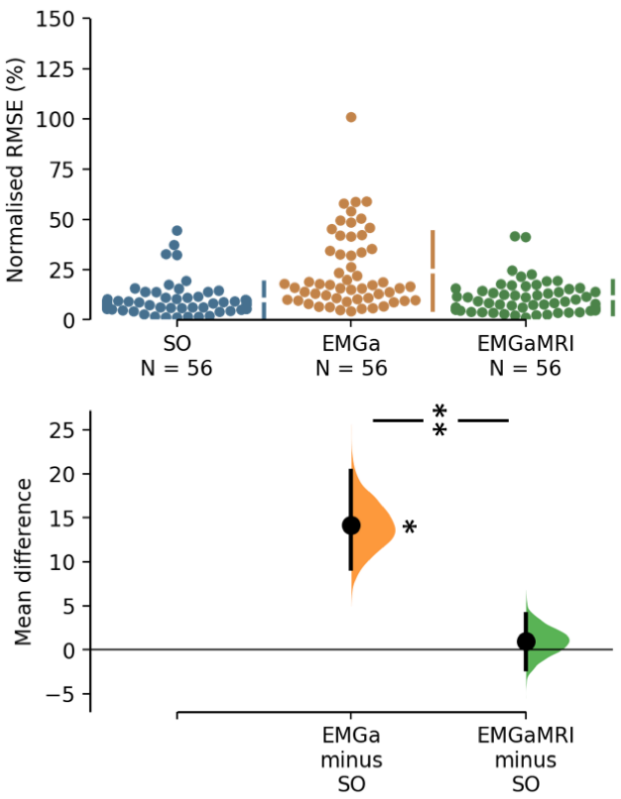

Fig. 11: Pooled normalised RMSE from the neuromusculoskeletal model with different neural solutions tracking inverse dynamics (ID) lateral bending net joint moments across all joints and trials. The RMSE values are the average across the 500 ms analysis period for each trial and joint level. These are shown in Cumming plots that present above the individual (solid marker), mean (gap between the vertical error bars) and standard deviation (vertical error bars) performance for SO (blue), EMGa (orange) and EMGaMRI (green) solutions. A total number of N = 56 data points corresponds to each of the seven (7) joint levels for each of the eight (8) trials. Below the mean difference and data distribution about the mean of the two EMG-assisted neural solutions (EMGa and EMGaMRI) from the SO solution is presented. Statistically significant difference of each EMG-assisted solution from the SO solution is shown by a single asterisk whilst significance between the two EMG-assisted solutions is indicated by a double asterisk

Normalised RMSE (NRMSE) of cervical spine net joint moment tracking across all joint levels and trials

Normalised RMSE (NRMSE) of cervical spine joint moments (C0-C1 to C6-C7) across individual joints and pooled from all joints are presented.

Additional information regarding the use of CEINMS in this study

1. *Re: Cost function's beta term and EMG tracking*
   The CEINMS solver minimises the error between the Inverse Dynamics (ID) estimated moments and the moments resulting from the simulated muscle forces. Muscle forces are simulated through the optimiser by constraining the 10 model MTUs to follow the experimental activations with the other 86 constrained to minimise the variability from their respective input signal (i.e. EMG signal from each functional quadrant). Thus the remaining 86 signals are not completely *"free"* to vary, but are provided an initial estimate (i.e. experimental EMG) and are then modulated to minimise variance from that signal and also generate the required force and subsequent joint torque to match the ID moments. The reason the beta term was set to zero was to test the hypothe-

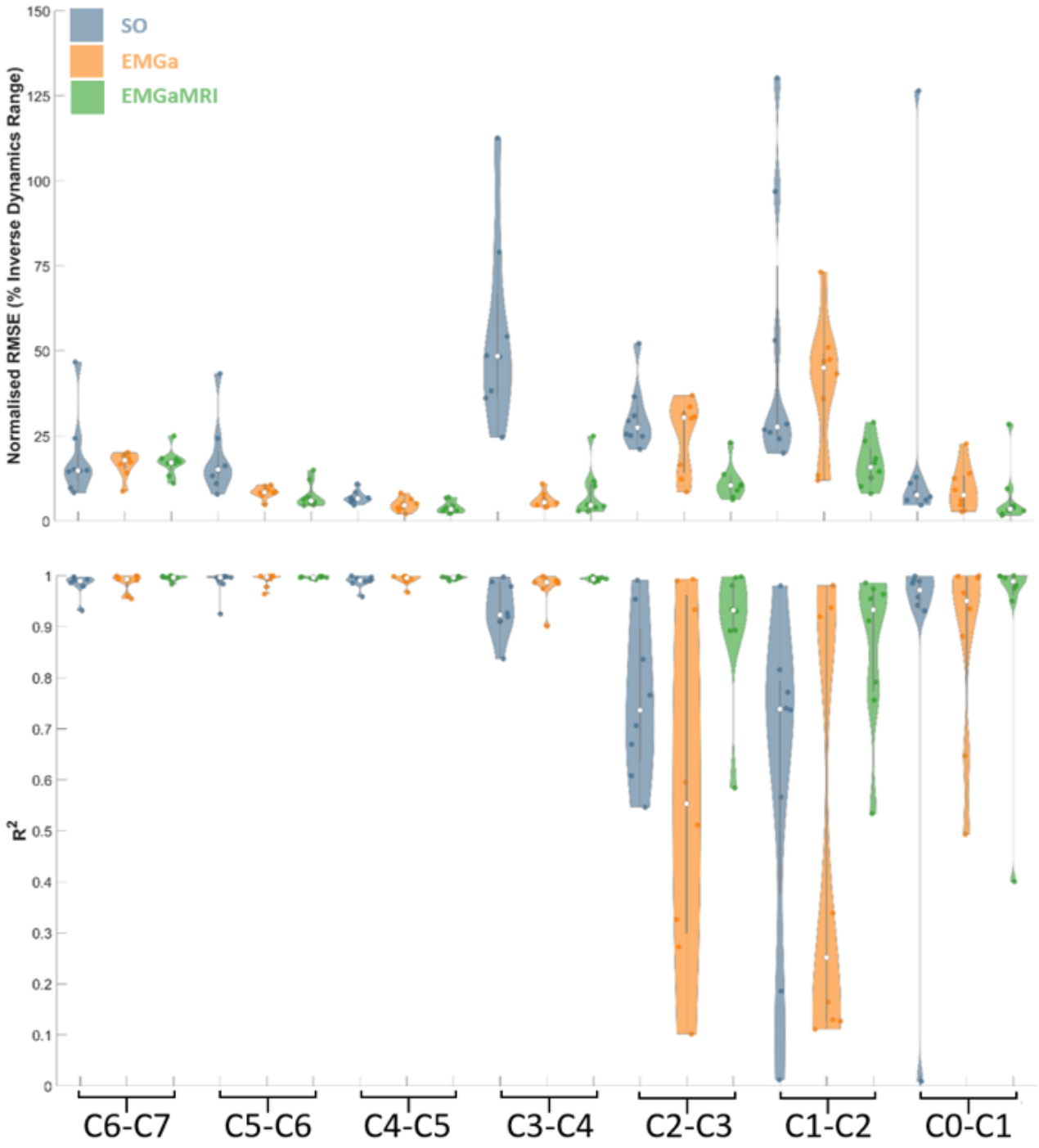

Fig. 12: Normalised RMSE (top) and R^2 (bottom) from the neuromusculoskeletal model with different neural solutions tracking inverse dynamics (ID) flexion/extension joint moments across different joints and trials. The RMSE and R^2 values are the average across the 500 ms analysis period for each trial. These are shown in violin plots that present individual (solid marker), mean (white marker) and density (coloured area shape) trial performance for SO (blue), EMGa (orange) and EMGaMRI (green) solutions. RMSE of each estimated joint moment is normalised to the range of the experimental joint moment (ID) of the respective joint and trial

sis that two sets of measurable data ID joint moments and EMG signals could be generated by a neuromusculoskeletal model without a priori cost function terms which was achieved. This approach should ensure the uniqueness of the solution, as the CEINMS solver uses a gradient descend *ipopt* algorithm (and not simulated annealing), and the problem is convex, being the sum of three quadratic functions.

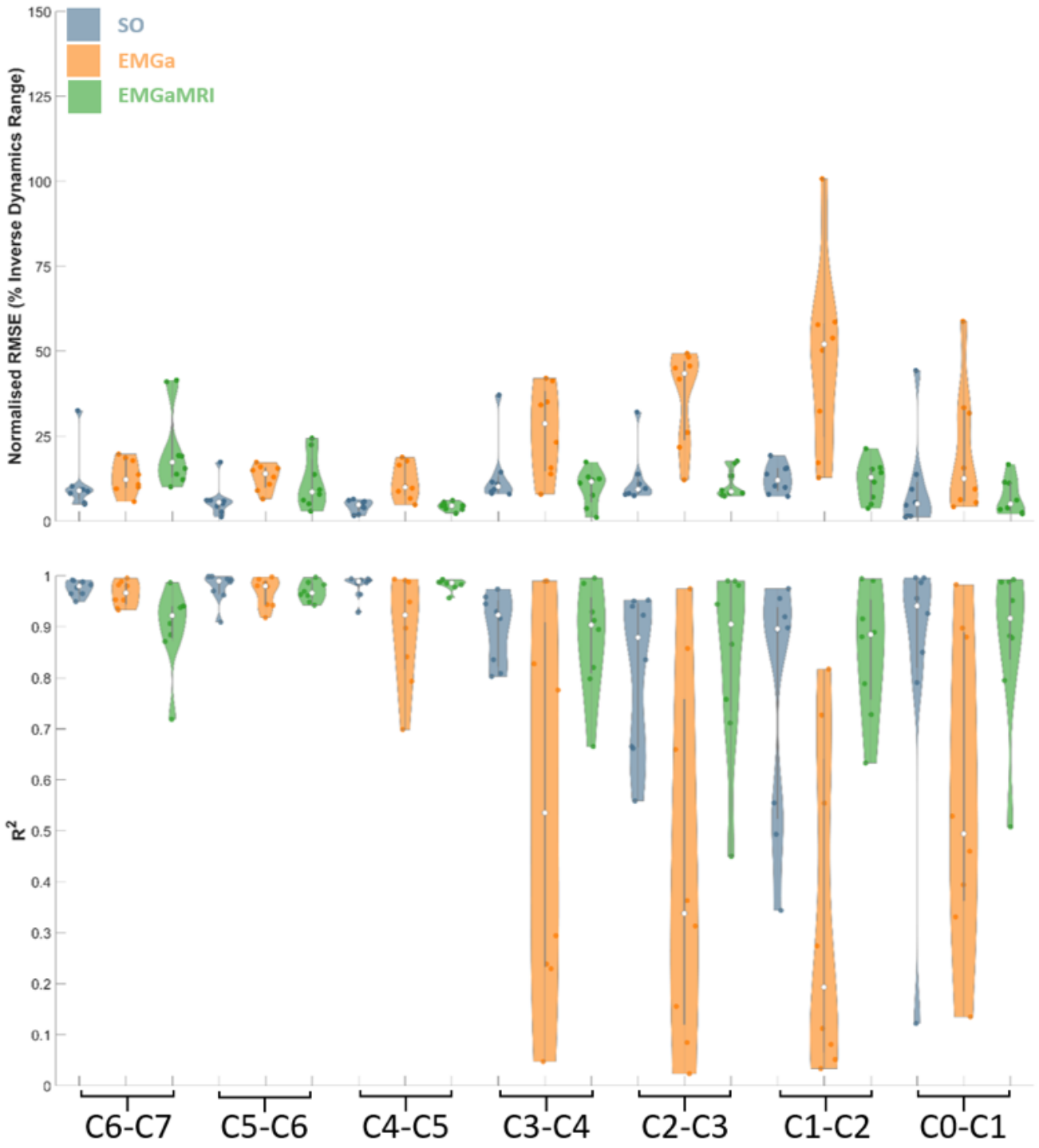

Fig. 13: Normalised RMSE (top) and R^2 (bottom) from the neuromusculoskeletal model with different neural solutions tracking inverse dynamics (ID) lateral bending joint moments across different joints and trials. The RMSE and R^2 values are the average across the 500 ms analysis period for each trial. These are shown in violin plots that present individual (solid marker), mean (white marker) and density (coloured area shape) trial performance for SO (blue), EMGa (orange) and EMGaMRI (green) solutions. RMSE of each estimated joint moment is normalised to the range of the experimental joint moment (ID) of the respective joint and trial

2. *Re: High frequency transitions and saturations of neural solution patterns and co-contraction indexes with SO* This is not observed often in previous CEINMS studies as SO works fairly well in gait, however, these issues were experienced at the shoulder [58], where contact forces were very variable. Also, those peaks usually

disappeared after calibrating the model. The SO was not run with a calibrated model in this study, as it would go beyond the scope of this paper.

SO was reported having more variables co-contractions indices in the past [18], showing that static optimisations favours solutions with minimal co-contractions. This stems from how SO is defined (i.e. minimisation of activation square), a criterion only based on external joint moment tracking. Additional criteria could be added to SO to alter the level of co-contractions, but they need to account for the surrounding environment and visual-vestibular system (e.g., preparation to an impact would increase neck stiffness) to result in physiologically plausible results. Conversely, EMG signals already encode all the information from the individual's central and peripheral nervous system, therefore automatically accounting for all these factors. Hence EMG-informed simulations directly inform the neuromusculoskeletal model with aspects of this sensory information as in-vivo EMG signals are used as input.

3. *Re: Differences between OpenSim Static Optimisation (SO) and the CEINMS SO solution*

   OpenSim uses SO modelling of ID moment as a constraint, it invokes reserve actuators to match ID joint moments if the musculoskeletal model is not able to do so. Previously, we have shown that OpenSim SO without reserve actuators and CEINMS EMGa produce the same size errors in ID moments tracking [60–62]. Second, the musculotendon model in OpenSim uses a rigid tendon and has no serial elastic muscle component. Therefore, CEINMS has none of these issues and we believe it is a much fairer comparison of SO, EMGa and EMGaMRI methods, which only tests differences in neural solutions using a consistent computational framework.